

# The Quantum Complexity of String Breaking in the Schwinger Model

Sebastian Grieninger  <sup>1,\*</sup> Martin J. Savage  <sup>1,†</sup> and Nikita A. Zemlevskiy  <sup>1,‡</sup>

<sup>1</sup>*InQuBator for Quantum Simulation (IQuS), Department of Physics,  
University of Washington, Seattle, WA 98195, USA*

(Dated: January 14, 2026)

String breaking, the process by which flux tubes fragment into hadronic states, is a hallmark of confinement in strongly-interacting quantum field theories. We examine a suite of quantum complexity measures using Matrix Product States to dissect the string breaking process in the 1+1D Schwinger model. We demonstrate the presence of nonlocal quantum correlations along the string that may affect fragmentation dynamics, and show that entanglement and magic offer complementary perspectives on string formation and breaking beyond conventional observables.

## I. INTRODUCTION

The formation of flux tubes, or chromoelectric strings, between color charges is a primary emergent feature of quantum chromodynamics (QCD) [1, 2]. The nonlinearity of the Yang-Mills Lagrange density [3], specifically the gluon self interactions, combined with quantum fluctuations, confine the lines of flux between static color charges into one-dimensional “strings” at modest separations. As the separation between a static quark and antiquark increases over an intermediate region, (compared to the confinement scale), the energy in the flux tube grows approximately linearly. At a certain distance a state of two hadrons (without a flux tube between them) becomes energetically favored. Such final states correspond to dynamical quarks from the vacuum rearranging themselves into baryon number  $\pm 1/3$  configurations around the static charges. This process is known as string breaking and is schematically shown in Fig. 1. In nature, string breaking occurs in high-energy collisions that produce high-multiplicity final states of strongly-interacting particles. While the dynamics of particle creation through string breaking, fragmentation and hadronization is well modeled [4–8], high-precision predictions in environments far from present-day experiments are challenging. Such predictions will be crucial at the future Electron-Ion Collider for determining nucleon partonic distributions, measuring gluon helicity contributions, and understanding diffractive dijet production [9, 10], as well as at the LHC for the discovery of new fundamental physics.

Significant theoretical and numerical results exist for string breaking processes (for recent overviews, see Refs. [11, 12]). String breaking can be probed, for example, through the electric potential between static charges as a function of their separation, as demonstrated in nu-

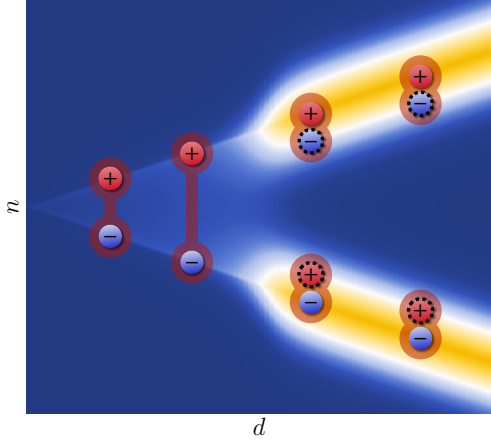


FIG. 1. *The formation of hadrons in the string breaking process.* The energy density, indicated by the heatmap color, shows the linearly increasing potential with the separation  $d$  of external charges (red and blue circles). A flux tube connecting the external charges develops (red tubes). At a certain separation, a pair of hadronic bound states is energetically favorable. Dynamical charges (circles with dashed border) are extracted from the vacuum to screen the external charges.

merous classic lattice-QCD simulations, e.g., Refs. [13–19]. More recently, advances in Hamiltonian simulation methods [20–27] and quantum spin chains [28–30] have enabled access to real-time dynamics and quantum observables, such as entanglement measures. These Hamiltonian approaches have been recently extended to two spatial dimensions [31–38]. In parallel, string breaking has received considerable experimental attention due to rapid progress in quantum technologies, and has been studied with quantum devices, including trapped-ion chains, Rydberg atom arrays, and superconducting qubit architectures, e.g., Refs. [39–45]. While both static and dynamical systems have been explored, deep connections with confinement and screening remain to be established.

The evolution of quantum complexity, reflecting physical dynamics and emergent phenomena, is a sensitive probe of the nature of physical processes, e.g., Refs. [46–

\* [segrie@uw.edu](mailto:segrie@uw.edu)

† [mjs5@uw.edu](mailto:mjs5@uw.edu)

‡ [zemlni@uw.edu](mailto:zemlni@uw.edu)

[65]. In this work, we investigate the behavior of multipartite entanglement and magic (nonstabilizerness) in the ground state of quantum electrodynamics in 1+1D (Schwinger model) with static background charges, as the system evolves from a confining string to isolated bound states. The Schwinger model shares features with 3+1D QCD that make it a natural testbed to study confinement, charge screening, string breaking, and few-body bound states (hadrons). For these reasons, it has been a focal point in developing quantum simulations of quantum field theories, e.g. Refs. [66–71]. We describe minimal simulation requirements for lattice studies of string breaking, and perform simulations to study the inherent quantum complexity (quantum correlations) in the wavefunction and reveal previously unknown structure. The measures of quantum complexity we have examined are found to change rapidly in the vicinity of string breaking, offering a complementary view of mechanisms involved in the formation of hadrons and the associated vacuum rearrangement.

## II. SIMULATING THE LATTICE SCHWINGER MODEL

### A. The Hamiltonian and Gauss's Law

In 1+1D with open boundary conditions (OBCs), the distribution of fermion charges completely constrains the gauge field through Gauss's law (see App. B for an analysis of boundary effects). Further, explicit gauge degrees of freedom are absent in axial gauge, leaving a non-local fermionic interaction in the Hamiltonian induced by the Coulomb potential. In the Kogut-Susskind formulation [72, 73], with staggered fermion discretization [74] and the Jordan-Wigner transformation [75, 76] to spin degrees of freedom, the lattice Hamiltonian of the Schwinger model is (for a derivation, see Ref. [73])

$$\hat{H}(d) = \frac{1}{4a} \sum_{n=1}^{N-1} \left( \hat{X}_n \hat{X}_{n+1} + \hat{Y}_n \hat{Y}_{n+1} \right) + \frac{m_{\text{lat}}}{2} \sum_{n=1}^N (-1)^n \hat{Z}_n + \frac{a}{2} \sum_{n=1}^{N-1} \left( \hat{E}_n + E_{\text{ext},n}(d) \right)^2, \quad (1)$$

where the lattice sites are labeled from  $n = 1$  to  $N$ , and the “link-sites” from  $n = 1$  to  $N - 1$ . Here,  $m_{\text{lat}} = m - \frac{g^2 a}{8}$  [77] is the chirally-improved (bare) fermion mass,  $m$  and  $g$  are the bare mass and coupling respectively and  $N$  is the number of staggered sites (corresponding to  $N_{\text{phys}} = N/2$  physical sites), and  $a$  is the (staggered) lattice spacing.<sup>1</sup> The last term specifies the nonlocal

<sup>1</sup> We have not included constant terms in Eq. (1). The physical lattice spacing is twice the staggered spacing,  $a_{\text{phys}} = 2a$ , and the number of physical lattice sites is half the number of staggered sites,  $N_{\text{phys}} = N/2$ . The physical length of the lattice is  $L = aN = a_{\text{phys}}N_{\text{phys}}$ .

fermionic interaction, where

$$\hat{E}_n = E_0 + g \sum_{k=1}^n \hat{Q}_k, \quad \hat{Q}_k = \frac{1}{2} \left( (-1)^k + \hat{Z}_k \right), \quad (2)$$

are the electric field between sites  $n, n+1$ , and the charge on site  $k$ , respectively. By convention, we set the background field  $E_0 = 0$ . The flux tube connecting two static external charges is represented by the external electric field  $E_{\text{ext},n}(d)$  [21].<sup>2</sup> A string of length  $d$  centered on the middle of the lattice is implemented by applying the external field

$$E_{\text{ext},n}(d) = g \text{ sign}(E) \cdot \Theta \left( \frac{d/a - 1}{2} - \left| n - \frac{N}{2} \right| + \epsilon \right), \quad (3)$$

where  $\Theta$  is the Heaviside step function and  $\epsilon$  is a small number. This represents a string created by a static external fermion at  $n = (N+1-d/a)/2$  and an antifermion at  $n = (N+1+d/a)/2$ .

In the absence of dynamical screening and vacuum rearrangement, the ground state of the Hamiltonian (1) encodes the rearrangement of the degrees of freedom in the vacuum in response to the insertion of static external charges. We refer to the ground state of  $H(d=0)$  as the “vacuum”, and study the behavior of the ground states of  $H(d)$  as a function of  $d$ .

### B. Minimal Lattice Requirements for Studies of String Breaking

In lattice simulations, physical states must be well-contained within the volume of the lattice, so that boundary and finite-volume effects can be quantified and systematically removed. The Compton wavelength  $l$  of excited states relevant to the physics of the process must be much smaller than the lattice size  $L$ . Furthermore, the pixelation (or “resolution”) of wavefunctions of low-lying states must be fine enough to resolve quantities of interest perturbatively close to their continuum values, meaning that  $l/a_{\text{phys}} \gg 1$ . Therefore, the lattice parameters must satisfy  $\frac{1}{L} \ll \Delta \ll \frac{1}{a_{\text{phys}}}$  for a lattice simulation to reliably capture the properties of the vacuum. Here  $\Delta \sim 1/l$  is the gap to the first excited state.<sup>3</sup> When simulating confining systems with static background charges separated by a distance  $d$  (or multiparticle states), boundary effects from the perturbations must be exponentially suppressed. This requires  $L \gg d$ .<sup>4</sup> A final restriction is that

<sup>2</sup> Instead of writing the electric field in terms of  $\hat{E}_n$  and  $E_{\text{ext},n}(d)$  one could also modify Gauss's law as explained in [20].

<sup>3</sup> As an example, for lattice QCD calculations at the physical values of the quark masses, with  $m_\pi \sim 140$  MeV, this condition implies that  $m_\pi L \gg 1$  and  $m_\pi a \ll 1$ . With a lattice spacing of  $a = 0.1$  fm, this gives  $m_\pi a \sim 0.07 \ll 1$ , and 64 lattice sites in each spatial direction gives  $m_\pi L \sim 4.5 \gg 1$ .

the distance between background charges is limited to integer multiples of the lattice spacing, i.e.,  $d = (2n - 1)a$ .

In this work, we have selected parameters for the spectrum and interactions to satisfy these conditions. As a starting point, we have chosen to work with the same Hamiltonian parameters used in Ref. [21] of  $g = 0.09$ ,  $m_{\text{lat}} = 0.045$ ,  $a = 1$  and  $N = 220$  staggered lattice sites ( $L = 110$ ) in Eq. (1). These choices, along with the vector meson mass  $M_v$  and the scalar meson mass  $M_s$ , are given in Table I.<sup>5</sup> These simulation parameters give  $M_v a_{\text{phys}} \sim 0.155$  and  $M_v L \sim 17.08$ , which satisfy conditions for perturbative finite volume and lattice spacing corrections. Further, the finite volume corrections are suppressed by  $\mathcal{O}(e^{-M_v L/2}) \sim 2 \times 10^{-4}$  for  $d = L/2$ . Continuum physics is identified from the  $a \rightarrow 0$ ,  $N \rightarrow \infty$  limit of the Hamiltonian in Eq. (1) with fixed  $m/g$  (with fixed  $m$  and  $g$ ). To approach the continuum with this physical parameter set, we have performed simulations with  $\{N, a\} = \{220, 1\}, \{440, \frac{1}{2}\}$  and  $\{880, \frac{1}{4}\}$ . These parameter choices keep the spatial extent of the lattice fixed to  $L = 110$ . The corresponding values of  $M_v$  and  $M_s$  are shown in Table I.

$N$	$a$	$m_{\text{lat}}$	$M_s$	$M_v$
220	1.00	0.04500	0.13647	0.07763
440	0.50	0.04551	0.13650	0.07919
880	0.25	0.04576	0.13651	0.07996

TABLE I. *Minimal lattice parameters for approaching the continuum limit in simulations of string breaking* For  $g = 0.09$  and  $m = 0.04601$  and a given system size  $N$  (first column) and lattice spacing  $a$  (second column), the third column displays the chirally-improved mass  $m_{\text{lat}}$ . The fourth and fifth columns give the scalar and vector meson masses,  $M_s$  and  $M_v$ , respectively.

### III. MEASURES OF QUANTUM COMPLEXITY AND GAUGE INVARIANCE

The distribution of quantum information in a state can provide insight into its underlying structure. In gauge theories, physically-meaningful measures of entanglement and quantum complexity must be gauge invariant, which restricts their definition to operations that preserve global charges. The ground state wavefunction

<sup>4</sup> For a simple system of charges, the potential experienced by a static charge in a 1D lattice volume  $L$  is the sum over image charge contributions [78–84]. For PBC,  $V^{\text{eff}}(d) = \sum_{n=-\infty}^{+\infty} V(|d + nL|)$ . Twisted boundary conditions can be helpful in minimizing the effects of the boundary, see e.g., Ref. [85], particularly i-PBCs for which the leading contributions to single-particle observables vanish.

<sup>5</sup> These masses are consistent with the scalar meson being a bound state of two vector mesons, with binding energy of  $2M_v - M_s \sim 0.0188$ .

$|\psi\rangle$  of the Schwinger model has vanishing total electric charge,  $Q = 0$ . However, reduced states have contributions from all charge sectors. For a bipartition of the lattice into regions  $A$  and  $B$ , the reduced density matrix  $\hat{\rho}_A$  has a block diagonal structure, with the blocks characterized by the charge within region  $A$ ,

$$|\psi\rangle = \sum_{Q,i} c_i^{(Q)} |\psi_A^{(Q,i)}\rangle \otimes |\psi_B^{(-Q,i)}\rangle ,$$

$$\hat{\rho}_A = \text{Tr}_B [\hat{\rho}_{AB}] = \sum_Q p_Q \hat{\rho}_A^{(Q)} , \quad (4)$$

where  $\hat{\rho}_{AB} = |\psi\rangle\langle\psi|$ . The block-diagonal form of  $\hat{\rho}_A$  allows the entanglement entropy to be decomposed into contributions from the charge sectors [86, 87] (see also Refs. [88–97] and references therein)

$$S(\hat{\rho}_A) = \sum_Q p_Q S(\hat{\rho}_A^{(Q)}) - \sum_Q p_Q \log_2 p_Q , \quad (5)$$

where  $S(\hat{\rho}) = -\text{Tr}[\hat{\rho} \log_2 \hat{\rho}]$  is the von Neumann entanglement entropy. By treating each charge sector separately, this quantity is naturally gauge invariant. This definition extends to other quantities, including mutual information (MI) and antiflatness. The MI is defined by

$$I(A : B) = S(\hat{\rho}_A) + S(\hat{\rho}_B) - S(\hat{\rho}_{AB}) , \quad (6)$$

using the definition in Eq. (5). The antiflatness for the same bipartition,  $\mathcal{F}_A(\hat{\rho}_A)$ , which provides a lower bound to the nonlocal magic [61],<sup>6</sup> becomes

$$\mathcal{F}_A(\hat{\rho}_A) = \sum_Q p_Q^2 \mathcal{F}_A(\hat{\rho}_A^{(Q)}) ,$$

$$\mathcal{F}_A(\hat{\rho}) = \text{Tr}\hat{\rho}^3 - (\text{Tr}\hat{\rho}^2)^2 = \text{Var}(\hat{\rho}^2) . \quad (7)$$

The Robustness of Magic (RoM) is defined by the minimum distance to the surface defined by stabilizer states,

$$R(\hat{\rho}) = \min_{\mathbf{x}} \left\{ \|\mathbf{x}\|_1 \mid \hat{\rho} = \sum_i x_i \hat{\rho}_{s_i} \right\} , \quad (8)$$

given by the 1-norm of the coefficients of the stabilizer density matrices  $\hat{\rho}_{s_i}$ . States that are elements of the stabilizer polytope will have  $x_i > 0$  and  $R(\hat{\rho}) = 1$ , while nonstabilizer states will have one or more  $x_i < 0$  and thus  $R(\hat{\rho}) > 1$ . As the trace of the density matrix is unity,  $R(\hat{\rho})$  measures the amount of negativity in the expansion coefficients,

$$\|\mathbf{x}\|_1 = 1 + 2 \sum_{i, x_i < 0} |x_i| , \quad (9)$$

<sup>6</sup> Results from small-qubit systems suggest the nonlocal magic is related to its lower bound by  $\mathcal{M}_2^{(NL)} = 4\mathcal{F}$ .

and hence provides a measure of the difficulty for classical simulation (more specifically,  $R(\hat{\rho}) - 1$ ). This is a faithful magic monotone for both pure states and mixed states. The nonlocal RoM (NL RoM) associated with subsystems  $A$  and  $B$ , is defined by a further minimization with respect to charge-preserving local unitary transformations in each region,

$$R_{AB}^{(NL)}(\hat{\rho}_{AB}) = \min_{\mathbf{x}, \boldsymbol{\theta}_A, \boldsymbol{\theta}_B} \left\{ \|\mathbf{x}\|_1 \mid \hat{U}_A(\boldsymbol{\theta}_A)\hat{U}_B(\boldsymbol{\theta}_B)\hat{\rho}_{AB}\hat{U}_A^\dagger(\boldsymbol{\theta}_A)\hat{U}_B^\dagger(\boldsymbol{\theta}_B) = \sum_i x_i \hat{\rho}_{s_i} \right\} \quad (10)$$

The transformations are constrained to preserve charge in each region for a gauge-invariant definition of  $R_{AB}^{(NL)}$ . For example, in the Schwinger model with the mapping to qubits as in Eq. (1), for regions  $A$  and  $B$  each having support on two qubits, the transformations are each parameterized by four angles

$$\hat{U}(\boldsymbol{\theta}) = e^{-i(\theta_0 \hat{Z}\hat{I} + \theta_1 \hat{I}\hat{Z} + \theta_2 \hat{Z}\hat{Z} + \theta_3 (\hat{X}\hat{X} + \hat{Y}\hat{Y}))}, \quad (11)$$

as opposed to the 15 angles for an arbitrary  $SU(4)$  transformation.

The recently identified Stabilizer Renyi Entropies (SREs) are calculable measures of the quantum magic in both pure and mixed states but they are not monotones for mixed states. The density matrix of a pure state  $|\psi\rangle$  may be written in the Pauli basis,

$$\hat{\rho} = |\psi\rangle\langle\psi| = \frac{1}{\mathbf{d}} \sum_{\hat{P}} \langle\psi|\hat{P}|\psi\rangle \hat{P} = \frac{1}{\mathbf{d}} \sum_{\hat{P}} c_{\hat{P}} \hat{P}, \quad (12)$$

where  $c_{\hat{P}} \equiv \langle\psi|\hat{P}|\psi\rangle$ , and  $\mathbf{d} = 2^{n_Q}$  for  $n_Q$  qubits. For pure states, the quantity  $\Xi_{\hat{P}} \equiv c_{\hat{P}}^2/\mathbf{d}$  is a probability distribution [50]. For a stabilizer state  $|\psi\rangle$ ,  $c_{\hat{P}} = \pm 1$  for  $\mathbf{d}$  commuting Pauli strings and  $c_{\hat{P}} = 0$  for the remaining  $\mathbf{d}^2 - \mathbf{d}$  strings [98]. The SREs measure the deviation from stabilizer states,

$$\mathcal{M}_\alpha(|\psi\rangle) = -\log_2 \mathbf{d} + \frac{1}{1-\alpha} \log_2 \left( \sum_{\hat{P}} \Xi_{\hat{P}}^\alpha \right), \quad (13)$$

with  $\mathcal{M}_2$  used in this work:<sup>7</sup>

$$\mathcal{M}_2 = -\log_2 \mathbf{d} \sum_{\hat{P}} \Xi_{\hat{P}}^2. \quad (15)$$

<sup>7</sup> The extension to mixed states is achieved by normalizing with respect to the partial probability,  $\sum_{\hat{P}}$ , e.g.,

$$\mathcal{M}_2^{\text{mixed}} = -\log_2 \left( \frac{\mathbf{d} \sum_{\hat{P}} \Xi_{\hat{P}}^2}{\sum_{\hat{P}} \Xi_{\hat{P}}} \right). \quad (14)$$

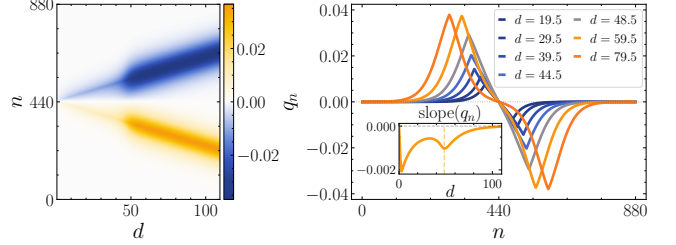


FIG. 2. The charge density  $q_n$  through the string breaking process. Left: the vacuum-subtracted charge density obtained with simulation parameters described in the text using  $N = 880$  and  $a = 1/4$ , as a function of position  $n$  and external charge separation  $d$ . Right: cross sections of the charge density for a selection of  $d$ 's. The inset shows the slope of the charge density at the center of the lattice, which has a local extremum at  $d = 48.5$ .

Nonlocal magic of a bipartition of a system into regions  $A$  and  $B$ , is the amount of magic that cannot be removed by local unitary transformations. Operationally, it is defined by

$$\mathcal{M}_\alpha^{(NL)}(|\psi\rangle) = \min_{\boldsymbol{\theta}_A, \boldsymbol{\theta}_B} \mathcal{M}_\alpha(U_A(\boldsymbol{\theta}_A)U_B(\boldsymbol{\theta}_B)|\psi\rangle), \quad (16)$$

for charge preserving transformations, as discussed around Eqs. (8) and (11). An upper bound for the nonlocal magic  $\mathcal{M}_2$  is found by writing the bipartitioned  $Q = 0$  ground state wavefunction as in Eq. (4) [99],

$$e^{-\mathcal{M}_2} = \sum_{\boldsymbol{\sigma}^{(1)}, \boldsymbol{\sigma}^{(2)}, \boldsymbol{\sigma}^{(3)}, \boldsymbol{\sigma}^{(4)}} c_{\boldsymbol{\sigma}^{(1)}} c_{\boldsymbol{\sigma}^{(2)}} c_{\boldsymbol{\sigma}^{(3)}} c_{\boldsymbol{\sigma}^{(1)} \boldsymbol{\sigma}^{(2)} \boldsymbol{\sigma}^{(3)}} \times c_{\boldsymbol{\sigma}^{(1)} \boldsymbol{\sigma}^{(2)} \boldsymbol{\sigma}^{(4)}}^* c_{\boldsymbol{\sigma}^{(1)} \boldsymbol{\sigma}^{(3)} \boldsymbol{\sigma}^{(4)}}^* c_{\boldsymbol{\sigma}^{(2)} \boldsymbol{\sigma}^{(3)} \boldsymbol{\sigma}^{(4)}}^* c_{\boldsymbol{\sigma}^{(4)}}^*, \quad (17)$$

where  $c_i = c_i^{(Q)}$  and products of  $\boldsymbol{\sigma}^{(s)}$  denote elementwise multiplication.

#### IV. RESULTS OBTAINED WITH CLASSICAL SIMULATIONS

We first show results obtained for classical local observables, conventionally studied in the context of string breaking. Figure 2 shows the vacuum-subtracted charge density  $q_n = \langle \hat{Q}_n \rangle/a$  as a function of the static charge separation  $d$ . With the simulation parameters described in the previous section, a small range of  $d$  captures significant changes in the structure of the ground state wavefunction. This rapid transition from strings to bound hadronic states takes place from  $d = 45 - 50$ . Dramatic changes in the charge distribution reflect the change from a single quarkonium-type state with a string between the static charges to a molecular-type state [100] of two mesons. As the external charges separate beyond this point, the mesons become isolated and the string between them vanishes.

The charge distribution between the static charges (right panel of Fig. 2) is observed to transition from

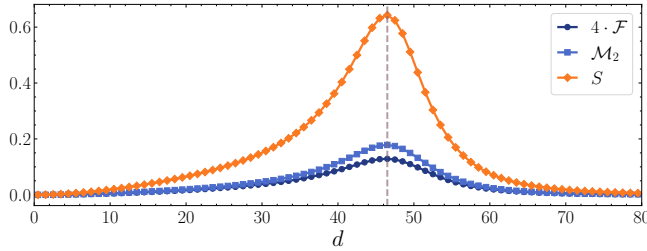


FIG. 3. Bipartite measures of entanglement and quantum complexity in string breaking. The symmetric bipartition entanglement entropy, antiflatness and the upper bound on the nonlocal  $\mathcal{M}_2$  using simulation parameters  $N = 880, a = 0.25, g = 0.09, m = 0.04601$ , as a function of separation between static sources in terms of physical spatial sites. These quantities all peak at  $d = 46.5$  (see Table II).

linear to curved with increasing  $d$ , consistent with the localization of the charge due to confinement. The inset shows the profile of the charge distribution. The width of this peak provides a measure of the separations over which the ground state structure changes from string-dominated to meson-dominated. The accompanying energy-momentum tensor components, as well as the chiral condensate and electric field, are discussed in App. D. These classical quantities have been well-studied in the context of string breaking (e.g., [20, 21]) and our results agree with existing literature.

One informative class of quantum complexity measures for these systems is the quantum correlations between bipartitions of the wavefunction about the center of the string. The entanglement entropy of such bipartitions has been studied previously (e.g., Ref. [22]), leading to important observations, including the reduced density matrix having the form of a thermal distribution at the point of string breaking [21]. For this half-lattice bipartition, we examine the (gauge-invariant) entanglement entropy using Eq. (5), the lower bound of the nonlocal magic using the antiflatness (Eq. (7)) and the upper bound of the nonlocal magic using Eq. (17). Figure 3 shows these quantities as a function of the separation between static charges. The previously identified peak in the entanglement entropy in the vicinity of string breaking is also observed in both the lower and upper bounds of nonlocal magic.<sup>8</sup> This result is consistent with the peak in nonlocal magic being driven by the entanglement between the regions.<sup>9</sup>

We conclude that during the transition from a string-dominated to a meson-dominated ground state structure, the nonlocal quantum magic of the bipartition increases above its vacuum value, and returns to its vacuum value

<sup>8</sup> Note that the peak in the charge slope happens at slightly larger distances compared to the peak of the entanglement entropy.

<sup>9</sup> Given the required size of the lattices, it is impractical to perform the minimization to determine the nonlocal magic. As a result, the bounds provide all of the accessible information about the bipartition nonlocal magic.

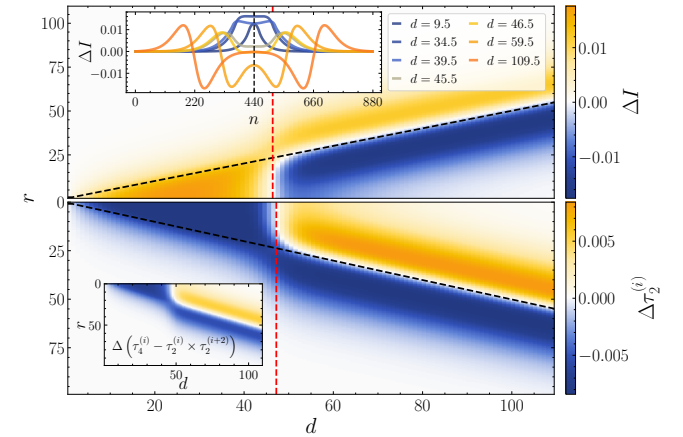


FIG. 4. Local and multipartite entanglement in string breaking. Top: the local vacuum-subtracted MI as a function of distance from the center  $r$  and external charge separation  $d$  for  $N = 880, a = 0.25, g = 0.09, m = 0.04601$ . The inset shows cross sections of the MI for a selection of  $d$ 's. Bottom: the vacuum-subtracted 2-tangle for the same parameters. The inset on the bottom panel shows the vacuum-subtracted 4-tangle. The black dashed lines indicate the peak of the charge distribution shown in Fig. 2. The red dashed lines correspond to the  $d$  where the respective quantity changes sign for the smallest  $r$ .

as the mesons separate. This is typical of a transition from long-range to short-range correlations. Moreover, this is consistent with the bipartition surface being (exponentially) insensitive to the presence of one or more mesons located in the bulk of the lattice, far from boundaries. This can be considered a magic barrier, analogous to those observed in the time evolution of nonequilibrium systems [101].

We probe quasi-local quantum correlations with the  $n$ -tangle  $\tau^{(n)}$  [102]

$$\tau_{(i_1 \dots i_n)}^{(n)} = |\langle \psi | \hat{Y}_{i_1} \otimes \dots \otimes \hat{Y}_{i_n} | \psi^* \rangle|^2, \quad (18)$$

where  $\hat{Y}_{i_k}$  is the Pauli matrix acting on qubit  $i_k$ . One interesting  $n$ -tangle to examine is  $\tau_{(i,i+1)}^{(2)}$  throughout the lattice, which provides a measure of nearest-neighbor entanglement. The lower panel of Fig. 4 shows the vacuum-subtracted  $\tau_{(i,i+1)}^{(2)}$  across the lattice as a function of the separation between the static charges. The nearest-neighbor entanglement is modified along the length of the string, which rapidly vanishes, changes sign in the vicinity of string breaking, then becomes confined into the mesons as they become isolated. This behavior is also evident in the vacuum-subtracted 4-tangle,  $\tau_{(i,i+1,i+2,i+3)}^{(4)} - \tau_{(i,i+1)}^{(2)} \tau_{(i+2,i+3)}^{(2)}$ , (inset of lower panel in Fig. 4) and in the vacuum-subtracted MI  $\Delta I$ , (upper panel of Fig. 4), both between adjacent spatial sites. The shape looks similar to  $\tau_{(i,i+1)}^{(2)}$ , indicating that much of, or all, the information

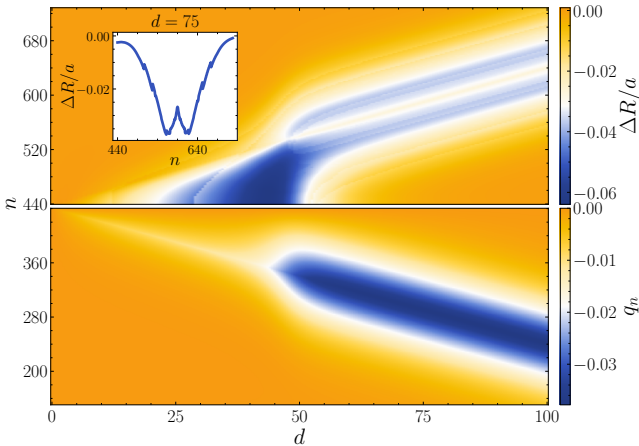


FIG. 5. *Internal structure of the outgoing meson revealed by the RoM.* Top: the vacuum-subtracted RoM of adjacent sites,  $\Delta R$  in units of  $a$ , shown for for  $n \geq 440$  as a function of  $d$ , for  $N = 880, a = 1/4$  as in Table I. The inset shows the behavior of  $\Delta R$  inside the meson region for  $d = 75$ . Bottom: the charge density  $q_n$  for  $n \leq 440$  for the same system.

is contained in the 2-tangle.<sup>10</sup> This suggests that (local) entanglement structure is limited to physical sites. There is a separation for which  $\tau_{(i,i+1)}^{(2)}$  vanishes along much of the string (indicated by the red dashed line), coinciding with the point of string breaking.<sup>11</sup> Notably, the zero that develops in  $\tau^{(2)}$  and the MI tracks the maximum of the charge distribution (shown with the black dashed line) after the string breaking. Deviations of  $\Delta I$  from 0 show the localization of correlations as a function of  $d$ , reflecting the underlying structure of string breaking and meson formation. The  $\Delta I$  in the middle region after string breaking arises from the nuclear force between the mesons, which vanishes when the mesons are sufficiently separated. It is interesting to note, that both the maximum and minimum of  $\Delta I$  are within the width of the meson defined by the charge profile peak (Fig. 2).

We use the RoM, defined in Eq. (8), as a measure of both local and nonlocal magic. Figure 5 shows the vacuum-subtracted RoM,  $\Delta R$  defined via Eq. (8) as

$$\Delta R(i) = R(i:i+3) - R_\Omega(i:i+3), \quad (19)$$

of four adjacent lattice sites,  $i, \dots, i+3$ , as a function of position and the separation of the external charges. Here  $R_\Omega$  denotes the value at  $d = 0$ . With increasing  $d$ , the deviation of  $\Delta R$  from zero increases along the string, becoming maximal at the point where the string breaks,

<sup>10</sup> We find the quantity  $\tau_{(i,i+1,i+2,i+3)}^{(4)} - c \tau_{(i,i+1)}^{(2)} \tau_{(i+2,i+3)}^{(2)} \rightarrow 0$  for  $c \approx 1.78$ .

<sup>11</sup> We observe that the nonlocal 4-tangle i.e.,  $\tau_{(N/2,N/2+1,i,i+1)}^{(4)} - \tau_{(N/2,N/2+1)}^{(2)} \tau_{(i,i+1)}^{(2)}$  vanishes everywhere for intervals away from the center (i.e., except for nearest neighbors).

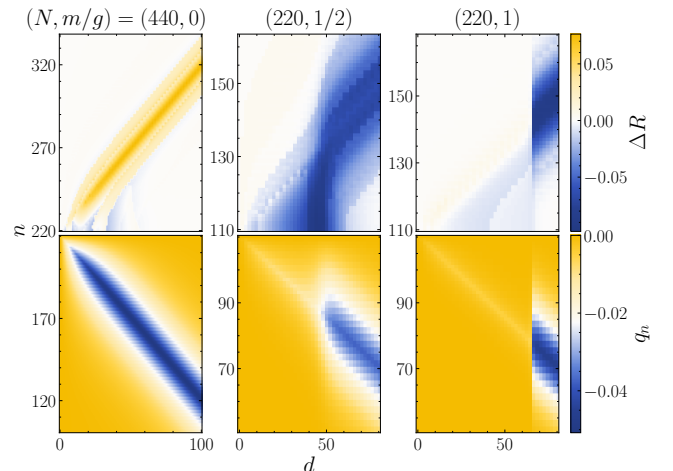


FIG. 6. *Dependence of string breaking on the fermion mass.* Left:  $m/g = 0$ , center:  $m/g = 1/2$  and right:  $m/g = 1$ . Top: the local vacuum-subtracted RoM as a function of  $d$  over half of the lattice  $n \geq N/2$  with  $a = 1$ . Bottom: the associated charge densities for  $n \leq N/2$  for the same parameters.

then decreasing rapidly as the mesons separate. The (local) RoM reveals structure in the string state before it breaks, and in the outgoing mesons.

The inset of Fig. 5 shows the distribution of  $\Delta R$  within the meson at  $d = 75$ . This suggests that moments of RoM distributions in hadronic structure calculations could be complementary probes of structure, in the same way that moments of the charge or axial distributions are computed (and measured experimentally). This shares similarities with the behavior of  $\Delta I$  within the meson (inset of top panel in Fig. 4). The lattice-spacing dependence of  $\Delta R$  is discussed in App. E. Compared to  $\tau^{(2)}$ ,  $\Delta R$  reflects the transition between strings and mesons less sharply.

Figure 6 shows  $\Delta R$  for different values of the fermion mass. The massless case has  $\Delta R > 0$  inside the isolated mesons, which is qualitatively different from the massive cases for which  $\Delta R < 0$ . String breaking is found to happen more abruptly for larger  $d$ , which is naively expected due to the increasing energy associated with screening the static charges. Furthermore, no string breaking is observed in the massless case, a result of dynamical fermions being easily “pulled” from the vacuum to screen the external charges. A more complete analysis can be found in App. E.

A novel class of quantum correlations in the context of string breaking are those between spatially-separated subregions [103]. The mutual information  $I(A : B)$ , defined in Eq. (6), provides a measure of both classical and quantum correlations between regions  $A$  and  $B$ . The left panel of Fig. 7 shows  $I(A : B)$  between spatial sites along the string with respect to the center of the system. The  $\Delta I$  is continuous along the string, peaking at the point of string breaking, and rapidly returning to vacuum values thereafter. Perhaps it is not surprising that the string provides long-distance classical or quantum correlations, or both, along the length of the string. It is also unsur-

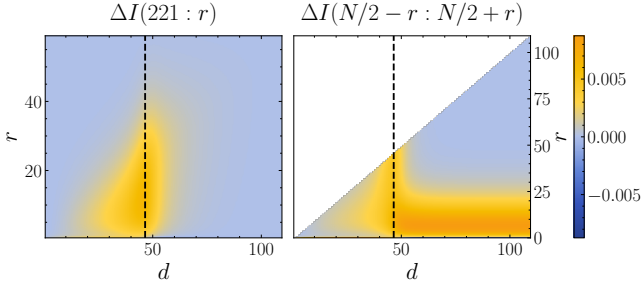


FIG. 7. *Mutual information in string breaking.* Left: The vacuum-subtracted MI,  $I(A : B)$ , between the spatial site (two staggered sites) adjacent to the midpoint of the lattice and the spatial site of the vertical axis as a function of the separation between the static charges, obtained with simulation parameters described in the text using  $N = 880$  and  $a = 1/4$ . The dashed line at  $d = 46.5$  indicates the peak of entanglement entropy, antiflatness and nonlocal magic, as shown in Fig. 3. Right: The corresponding vacuum-subtracted MI between the spatial sites of the static charges.

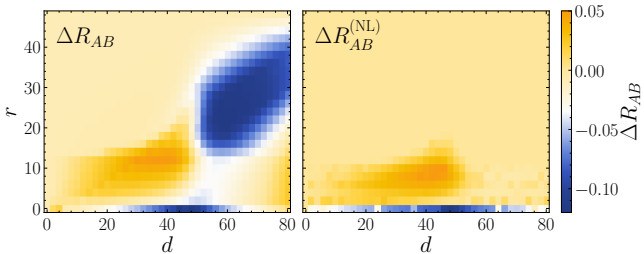


FIG. 8. *Nonlocal quantum correlations in string breaking as measured by the NL RoM.* Left: the RoM of disjoint regions,  $\Delta R_{AB}$ , where region  $A$  is at the center of the lattice and region  $B$  is distance  $r$  away. The vacuum value ( $d = 0$ ) and the values as  $r \rightarrow \infty$  are subtracted. The system parameters  $N = 220$ ,  $a = 1$ ,  $m_{\text{lat}} = 0.045$ ,  $g = 0.09$  are used as in Table I. Right: the NL RoM,  $\Delta R_{AB}^{\text{NL}}$  for the same system parameters.

prising that these correlations vanish as the system transitions to isolated mesons. However, the transition region extends (at least) over the range of the nuclear force between the mesons.<sup>12</sup> The vacuum-subtracted MI over the interval between the two external charges, where region  $A$  is fixed at the position of the first external charge, is shown in the right panel of Fig. 7. Analogous to the left panel, it is continuous along the string and its extent peaks near the string breaking. At larger  $d$ , it is nonzero over the extent of the meson at the reference static charge.

The left panel of Fig. 8 shows the RoM  $\Delta R_{AB}$  between disjoint subsystems on the lattice as a function of the distance between the regions  $r$ . Region  $A$  is at the center

of the lattice,  $A = (N/2 + 1, N/2 + 2)$ , and region  $B$  is distance  $r$  away,  $B = A + (r, r + 1)$ . We define this quantity with a different vacuum subtraction to that in Eq. (19),

$$\Delta R_{AB} = R(A, B) - R_{\infty}(A, B) - R_{\Omega}(A, B) , \quad (20)$$

where  $R_{\infty}$  denotes the quantity evaluated as  $r \rightarrow \infty$  and  $R_{\Omega}$  denotes the value at  $d = 0$  (as before). The reason for this is that the wavefunction is modified at the center of the lattice before string breaking, providing a modification in  $R$  for all values of  $i$ . The isolated meson is visible in  $\Delta R_{AB}$ , as is the string breaking. Unlike the MI, the RoM shows a different structure along the string in the vicinity of the string breaking. In particular, it exhibits a localized rapid change of sign at the point of string breaking (as identified by the vanishing of the vacuum-subtracted 2-tangle and other measures). This is consistent with the center being the location of the most “restructuring” of the wavefunction. This rapid increase in charge density (also seen in Fig. 2) coincides with the “hot spot” in the left panel of Fig. 8. Interestingly, the NL RoM (defined in Eq. (10)) shows similar, but more localized behavior to the MI (cf. Fig. 7). The outgoing meson “track” vanishes in the NL components of the RoM (right panel of Fig. 8), suggesting that NL quantum information is only encoded in the string state. The presence of NL RoM establishes a link between spatially extended physical objects (strings) and nonlocal quantum complexity independent of basis choice. These purely quantum correlations, absent from traditional models of hadronization, could imprint themselves into final states in high-energy collisions.

## V. SUMMARY AND DISCUSSION

Understanding confinement and developing robust predictive capabilities for the resulting dynamical phenomena, such as fragmentation and hadronization, remains a long-standing challenge. On the path to scientific discovery in high-energy and nuclear physics, techniques from quantum information science are now being used to address this challenge. We have performed classical simulations of string formation and breaking in the (Abelian) Schwinger model, focusing on quantum complexity beyond bipartite entanglement entropy. Measures of both local and nonlocal quantum complexity are found to provide distinct and complementary probes of the mechanism of string formation and breaking.

We find that quantities, such as the nonstabilizerness and multipartite entanglement of contiguous subsystems, exhibit rapid variations in the vicinity of string breaking, in contrast to classical quantities like energy density. Importantly, nonlocal quantum complexity (as measured by both the MI and the NL RoM) is found along the string, with classical correlations appearing to be somewhat longer range than the quantum correlations. Both vanish abruptly after string breaking. This shows that

<sup>12</sup> It would be interesting to examine the behavior of  $I(A : B)$  and  $\Delta R_{AB}^{\text{NL}}$  for a system with unnatural scattering parameters, to determine whether it is the string-breaking scale, the nuclear force or the scattering parameters that determine the change in the measures as a function of separation.

both classical and quantum correlations develop during string breaking, but suggests that the longer distance correlations are predominately classical. Unfortunately, our computations of nonlocal measures of complexity are limited to small systems due to the resources required for minimizations in the subregions, along with considerations of the stabilizer polytope. We have not computed measures of higher-body nonlocal magic, for the reasons stated above, and cannot rule them out.

The quantum complexity exhibits sharp changes in the transition from flux tubes to isolated hadronic bound states, akin to phase transitions [21]. We expect that the behavior of quantum complexity in a dynamical simulation of string breaking will help answer questions difficult to investigate with statics alone. For instance, the dynamics of charge extraction from the vacuum can shine light on the mechanisms governing confinement. Such a study would require the simulation of wavepacket evolution [70, 104, 105] or the use of a time-dependent Hamiltonian [106, 107]. Applying our techniques to dynamical settings, to non-Abelian theories and to higher-dimensional systems will be illuminating. We also anticipate that the quantum complexity in string breaking will be imprinted in the final states of collisions of hadrons and nuclei. Analyses are already underway at the LHC to quantify entanglement and magic in top-anti-top production events [108, 109]. If detected in experiment, the hierarchies of these correlations and their (non)locality may affect modeling of fragmentation and hadronization.

## ACKNOWLEDGMENTS

We would like to thank Roland Farrell, Henry Froland, Tobias Haug, Dima Kharzeev, Eliana Marroquin and Caroline Robin for helpful discussions. This work was supported, in part, by U.S. Department of Energy, Office of Science, Office of Nuclear Physics, InQubator for Quantum Simulation (IQuS) under Award Number DOE (NP) Award DE-SC0020970 via the program on Quantum Horizons: QIS Research and Innovation for Nuclear Science. S.G. was supported in part by the U.S. Department of Energy, Office of Science, Office of Nuclear Physics, Grants No. DE-FG02-97ER-41014 and in part by a Feodor Lynen Research fellowship of the Alexander von Humboldt foundation. This work was also supported, in part, by the Department of Physics and the College of Arts and Sciences at the University of Washington. This work was enabled, in part, by the use of advanced computational, storage and networking infrastructure provided by the Hyak supercomputer system at the University of Washington. This research used resources of the National Energy Research Scientific Computing Center (NERSC), a Department of Energy Office of Science User Facility using NERSC award NP-ERCAP0032083. This research was done using services provided by the OSG Consortium [110–113], which is supported by the National Science Foundation awards

#2030508 and #1836650. We have made use of the ITensor library for tensor network computations [114–116].

## Appendix A: Analysis of lattice spacing artifacts

On a staggered lattice, the electric field points from antifermion to fermion sites. For our choice of parameters, odd sites correspond to fermions and even sites to antifermions. Hence, for  $N/2$  even the middle link is between an antifermion and fermion site and the external electric field should point to the right (i.e., larger indices in the chain). This corresponds to our  $d = a$  configuration. For  $d = 3a$ , the opposite configuration is supported. Note that both the  $d = a$  and  $d = 3a$  configuration belong to the same physical site. This implies that we should average over neighboring configurations to obtain physical sites, i.e., we average  $d = a$  and  $d = 3a$ ,  $d = 5a$  and  $d = 7a$ , etc. The averaged configurations then correspond to physical separations of  $d = 2a, 6a$ , etc. In the continuum, there is no distinction between fermion and antifermion sites and the results obtained for either direction of the electric field should be equal. Hence, a good proxy for the impact of lattice artifacts is to compare the results obtained for both directions of the external electric field. This is exemplified in Fig 9. In the first three panels, we keep  $L = Na$  fixed and decrease the lattice spacing from  $a = 1$  to  $a = 1/4$ . For  $a = 1$  there is a clear difference in the entanglement entropy for the two different directions of the  $E_{\text{ext}}$ . In fact, the  $S_+$  curve even turns negative at small  $d$ . The two curves converge in the  $a \rightarrow 0$  limit. To account for the difference at finite lattice spacing, we average  $S$ ,  $\mathcal{F}$  and  $\mathcal{M}_2$  over the two different directions of the electric field as shown in the fourth plot in Fig 9.

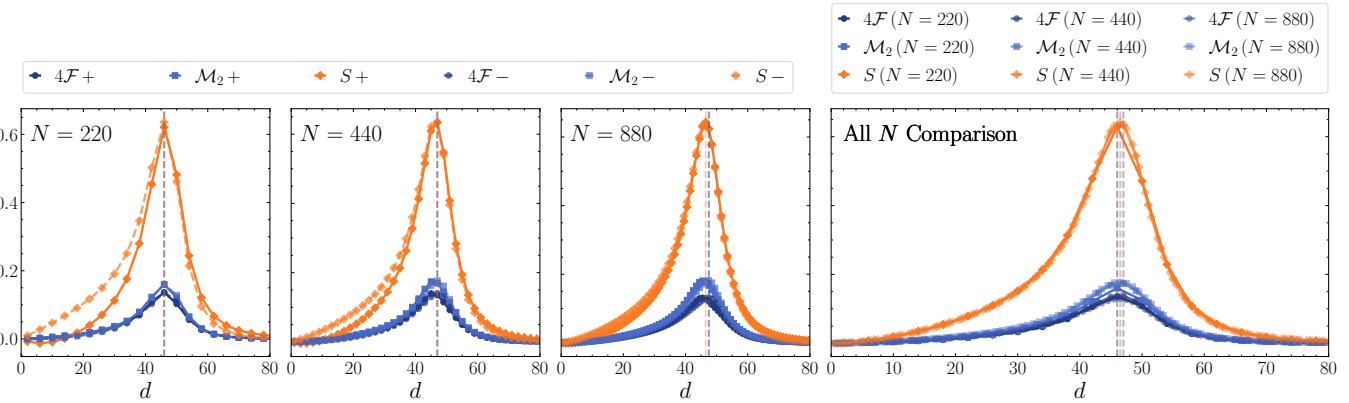


FIG. 9. Bipartite measures of entanglement and quantum complexity as a function of  $N, a$  for  $(N, a) = (220, 1), (440, 1/2)$ , and  $(880, 1/4)$ . The antiflatness  $4\mathcal{F}$ , the upper bound to the nonlocal magic  $\mathcal{M}_2$ , and the entanglement entropy  $S$  are shown for both orientations of the external field  $E_{\text{ext}} = -$  and  $E_{\text{ext}} = +$ . The right panel shows the average over the orientations of  $E_{\text{ext}}$  for all  $N, a$ . The locations of the peaks for each measure are given in Table II.

		Peak position								
Measure	N = 220, a = 1			N = 440, a = 1/2			N = 880, a = 1/4			avg.
	$E_{\text{ext}} = -$	$E_{\text{ext}} = +$	avg.	$E_{\text{ext}} = -$	$E_{\text{ext}} = +$	avg.	$E_{\text{ext}} = -$	$E_{\text{ext}} = +$	avg.	
$\mathcal{F}$	46.0	46.0	46.0	47.0	45.5	46.25	45.5	47.5	46.5	
$\mathcal{M}_2$	46.0	46.0	46.0	47.0	45.0	46.0	45.5	47.5	46.5	
$S$	46.0	46.0	46.0	47.0	47.0	47.0	46.5	46.5	46.5	

TABLE II. The values of  $d$  for which the measures (left column) reach their maximum value, for parameters in Table I and both orientations of the external field  $E_{\text{ext}} = -$  and  $E_{\text{ext}} = +$ , and the average of the two orientations.

## Appendix B: OBC vs PBC

With the parameters chosen as described in Sec. II B, the effect of boundaries and finite volume on the physics of the simulation is exponentially suppressed. As a result, the choice of boundary conditions should not impact the results of the computations.<sup>13</sup> With OBCs, dynamical gauge field degrees of freedom can be eliminated from the

<sup>13</sup> OBCs are highly preferred due to the inefficiency of standard MPS in representing periodic states [117].

theory, resulting in long range fermionic interactions through a linear potential. In PBCs, there is a single gauge field degree of freedom, the “zero mode”, whose dynamics is not constrained by Gauss’s law. We follow the approach of Refs. [105, 118, 119], where the gauge field zero mode is truncated to a single state and zero mode dynamics is not considered. This approximation is valid for low-energy dynamics, and corrections are suppressed by  $L$ . The Hamiltonian is modified from Eq. (1):

$$\begin{aligned} \hat{H}_{\text{PBC}}(d) = & \frac{m_{\text{lat}}}{2} \sum_{n=1}^N (-1)^n \hat{Z}_n - \frac{g^2}{2} \sum_{n=1}^N \left\{ \sum_{s=1}^{N_{\text{phys}}} \left( s - \frac{s^2}{N} \right) \left( 1 - \frac{\delta_{s,N_{\text{phys}}}}{2} \right) \hat{Q}_n \hat{Q}_{n+s} + 2 \sum_{k=1}^{N-1} \frac{N-k}{N} E_{\text{ext},n}(d) \hat{Q}_{n+k} \right\} \\ & + \frac{1}{2} \sum_{n=1}^{N-1} \left( \hat{X}_n \hat{X}_{n+1} + \hat{Y}_n \hat{Y}_{n+1} \right) + \frac{1}{2} (-1)^{N_{\text{phys}}+1} \left( \hat{X}_N \hat{X}_1 + \hat{Y}_N \hat{Y}_1 \right). \end{aligned} \quad (\text{B1})$$

With the lattice parameters chosen as in Table I, we observe a difference in the string breaking process between PBCs and OBCs with the same system size  $N$ . As shown in Fig. 10, the string breaks at a larger separation  $d$  for PBCs. This is attributed to image charge effects in PBCs that are absent in OBCs,<sup>14</sup> indicating that these calculations are not far into regime prescribed in Sec IIB. The boundary effects, both from the lattice boundary in OBCs and image charges in PBCs, extend into the lattice volume by a length scale set by the lightest hadron mass. As expected, the charge density of the OBC and PBC vacua determined by DMRG agree in the bulk.

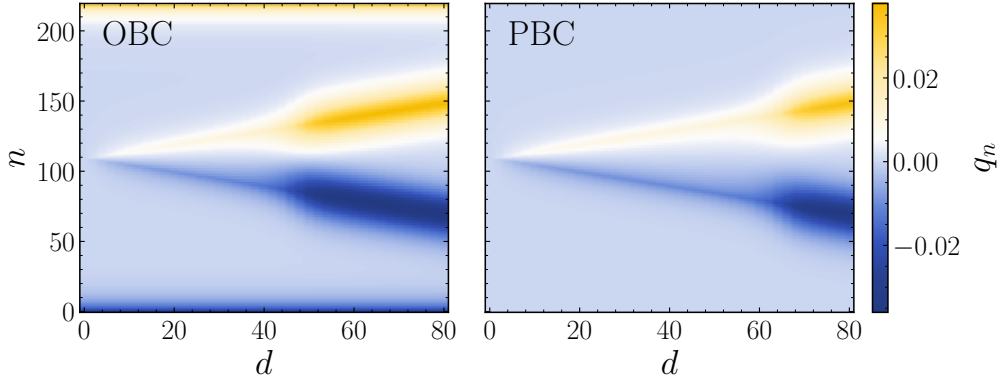


FIG. 10. The charge density for OBC (left) and PBC (right)  $N = 220, a = 1, m_{\text{lat}} = 0.045, g = 0.09$  as in Table I.

### Appendix C: Charge Rearrangement During String Breaking

During string breaking, charge is extracted from the vacuum to screen the heavy charges, so it is natural to study the rearrangement of charge. Considering a bipartition of the system at the center of the lattice, the ground state wavefunction may be written as in Eq. (4). The charge rearrangement may be examined through the effect that screening has on the sector weights  $p_Q$ . At  $d = 0$ , the ground state is the lowest-lying state with total  $Q = 0$ , so that only charge-neutral terms appear in Eq. (4). Introducing background charges causes the weights  $p_Q$  to change, as the vacuum rearranges to the new lowest-energy state. When the background charges are far apart, effects near the bipartition are exponentially suppressed by confinement, so only the light degrees of freedom that do not participate in screening contribute to  $p_Q$ . The half-lattice charge changes by one. In the following,  $|Q^+\rangle$  denotes an external charge of +1, and  $|q\rangle$  denotes the (reduced) state of the half-lattice. The changes for that the lowest several charge sectors experience are

$$\begin{aligned} |Q^+\rangle \otimes |q=0\rangle &\rightarrow |Q^+e^-\rangle \otimes |q=+1\rangle, \\ |Q^+\rangle \otimes |q=+1\rangle &\rightarrow |Q^+e^-\rangle \otimes |q=+2\rangle, \\ |Q^+\rangle \otimes |q=-1\rangle &\rightarrow |Q^+e^-\rangle \otimes |q=0\rangle, \\ |Q^+\rangle \otimes |q=+2\rangle &\rightarrow |Q^+e^-\rangle \otimes |q=+3\rangle, \\ |Q^+\rangle \otimes |q=-2\rangle &\rightarrow |Q^+e^-\rangle \otimes |q=-1\rangle, \end{aligned} \quad (\text{C1})$$

<sup>14</sup> This is verified by considering a larger lattice with the same lattice spacing, where the image charges are further away and the string breaks at an  $d$  closer to OBCs.

and similarly for the  $|Q^-\rangle$  region. In other words, for the half of the lattice with the  $|Q^+\rangle$  external charge,  $p_{q=0} \rightarrow p_{q=+1}$ ,  $p_{q=+1} \rightarrow p_{q=+2}$ , etc.

In our formalism, string breaking may be observed in two equivalent ways, with the external field pointing toward  $n = 0$ ,  $E_{\text{ext}} = -$ , and toward  $n = N - 1$ ,  $E_{\text{ext}} = +$ .<sup>15</sup> Fig. 11 shows the rearrangement of  $p_Q$  for the two choices of  $E_{\text{ext}}$ .

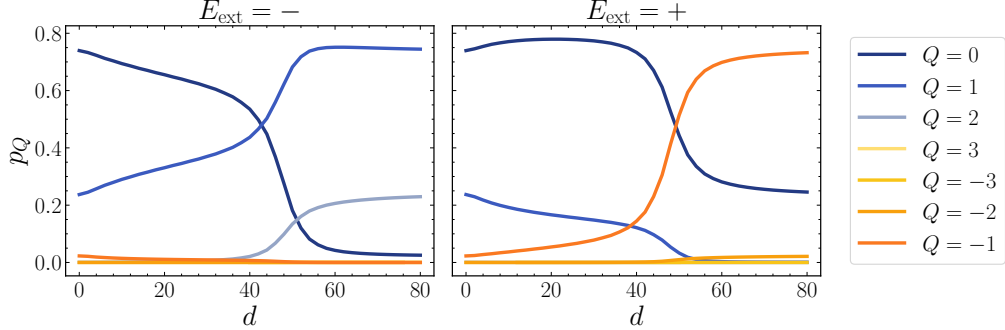


FIG. 11. The charge sector weights  $p_Q$  as a function of external charge separation  $d$  for the two different orientations of the external field,  $E_{\text{ext}} = -$  and  $E_{\text{ext}} = +$ . The system parameters  $N = 220$ ,  $a = 1$ ,  $m_{\text{lat}} = 0.045$ ,  $g = 0.09$  are used as in Table I.

Physical quantities should not depend on the choice of  $E_{\text{ext}}$  orientation. However, we observe that the  $p_Q$  transitions do not follow Eq. (C1) exactly, and behave differently for the different orientations of the electric field. OBCs generate a charge asymmetry along the lattice from the ordering of fermions and antifermions (seen in Fig. 10), created by configurations localized around the boundaries. These boundary charge densities present a challenge for interpreting global measures of entanglement and quantum complexity, that have sensitivity to the entire lattice or half-lattices. This effect is responsible for the differences with Eq. (C1) and the asymmetry of the left and right panels of Fig. 11.

Attempts to compensate for boundary effects by inserting image charges did not reduce the asymmetry between the two panels of Fig. 11. Switching to PBCs as described in App. B introduces a second entangling surface, and makes Eq. (C1) superficially true due to symmetry. Considering a subregion of the bipartition that does not include the external boundary has similar issues. As seen in the left panels of Fig. 9 and Table II, these effects do not go away with reduced lattice spacing, as naively expected. For this reason, it is important to consider measures of quantum complexity that are insensitive to boundary effects.

#### Appendix D: Additional Classical Observables

Figure 12 shows the chiral condensate and the electric field as functions of position  $n$  and separation of external charges  $d$ . The chiral condensate  $C$  is defined as

$$C_n = \frac{(-1)^n}{2a} \langle Z_n \rangle , \quad (\text{D1})$$

and the electric field  $E_n$  is given in Eq. (2). The relevant components of the energy-momentum tensor are given

<sup>15</sup> The configuration  $E_{\text{ext}} = -$  corresponds to an external fermion on the left half of the lattice, and an antifermion on the right, and vice-versa for  $E_{\text{ext}} = +$ .

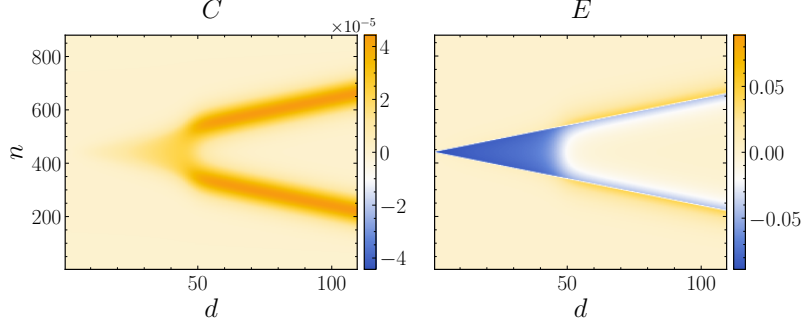


FIG. 12. The vacuum-subtracted chiral condensate (left panel) and electric field (right panel) obtained with simulation parameters described in the text using  $N = 880$  and  $a = 1/4$ .

by [120]

$$\hat{T}_n^{00} = \frac{1}{2a} \left( \hat{K}_n + \hat{K}_{n-1} + m(-1)^n \hat{Z}_n + \frac{a}{2} (\hat{E}_{\text{tot},n}^2 + \hat{E}_{\text{tot},n-1}^2) \right), \quad (\text{D2})$$

$$\hat{T}_n^{11} = \frac{1}{2a} \left( \hat{K}_n + \hat{K}_{n-1} - \frac{a}{2} (\hat{E}_{\text{tot},n}^2 + \hat{E}_{\text{tot},n-1}^2) \right), \quad (\text{D3})$$

Here,  $\hat{K}_n = \frac{1}{4a} (\hat{X}_{n+1} \hat{X}_n + \hat{Y}_{n+1} \hat{Y}_n)$  is the kinetic term,  $\hat{E}_{\text{tot},n} = \hat{E}_n + E_{\text{ext},n}$  and all indices that are smaller than 1 or larger than  $N$  are zero with open boundary conditions. The third component  $\hat{T}_n^{01}$  vanishes in the ground state. The energy density  $\varepsilon$  and the pressure  $p$  are related to the energy-momentum tensor components by

$$\hat{\varepsilon}_n = \frac{1}{2} \left( \hat{T}_n^{00} - \hat{T}_n^{11} \pm \sqrt{(\hat{T}_n^{00} + \hat{T}_n^{11})^2 - 4(\hat{T}_n^{01})^2} \right), \quad (\text{D4})$$

$$\hat{p}_n = \hat{\varepsilon} - (\hat{T}_n^{00} - \hat{T}_n^{11}), \quad (\text{D5})$$

where the positive sign is chosen for  $\hat{T}_n^{00} + \hat{T}_n^{11} \geq 0$  and the negative sign otherwise.

We computed the energy density and pressure, which are displayed in Fig. 13. The results are consistent with those

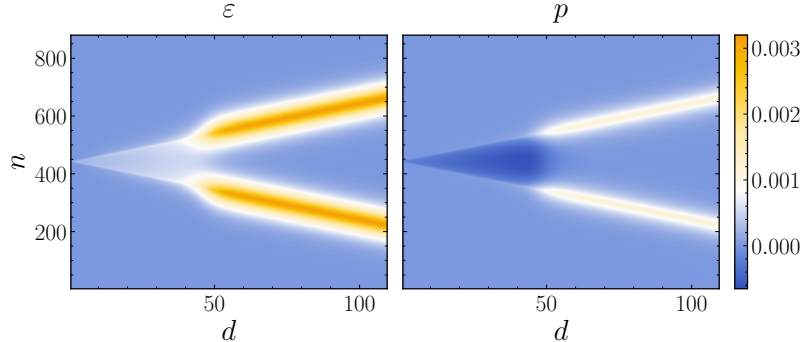


FIG. 13. Components of the vacuum-subtracted energy-momentum tensor obtained with simulation parameters described in the text using  $N = 880$  and  $a = 1/4$ . The left panel shows the energy density  $\varepsilon$ , while the right panel shows the pressure  $p$ .

given in Ref. [21], but with finer resolution of the string-breaking process. The pressure distribution is particularly interesting. The pressure is seen to become increasingly negative with increasing static-charge separation, and then revert rapidly to the vacuum value after string breaking. In contrast, the pressure within the mesons rapidly increases from its vacuum value after string breaking.

#### Appendix E: Supplemental Quantum Complexity Results

A natural quantity to consider is the behavior of magic in the continuum as  $a \rightarrow 0$ . In principle, this could be studied by computing the RoM of a region of fixed physical volume, (i.e.,  $L = N_{\text{phys}}a = \text{const.}$ ). However, the number of stabilizer states over which the RoM must be computed grows superexponentially [121], and is intractable for more

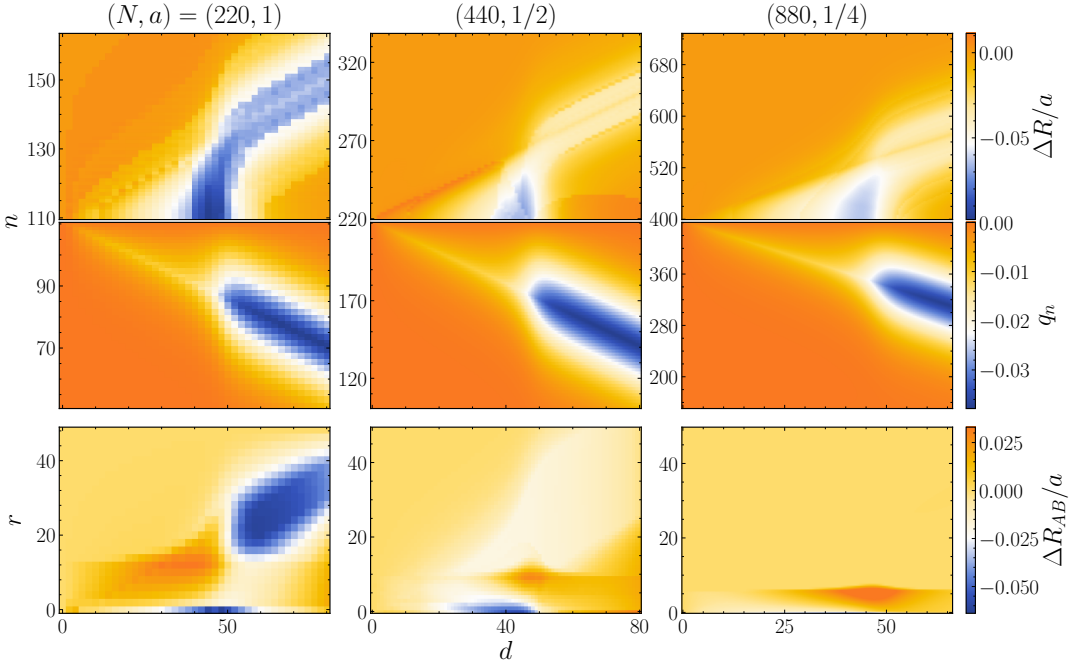


FIG. 14. The dependence of the RoM on system size and lattice spacing. Top: The vacuum-subtracted RoM of adjacent sites,  $\Delta R$  for a selection of system sizes and lattice spacings  $(N, a) = (220, 1)$  (left),  $(440, 1/2)$  (center), and  $(880, 1/4)$  (right). The RoM is plotted in units of  $a$  for half of the lattice  $n \geq N/2$  as a function of external charge separation  $d$ . The system parameters from Table I are used. Middle: the associated charge densities for half of the lattice  $n \leq N/2$ . Bottom: the RoM of disjoint regions,  $\Delta R_{AB}$ , with region  $A$  at the center of the lattice and region  $B$  a distance  $r$  away. The vacuum value ( $d = 0$ ) and the value as  $r \rightarrow \infty$  are subtracted. The RoM is plotted in units of  $a$  for the same system parameters.

than 8 qubits [58]. Instead of this, we compute the RoM for a subregion of fixed size, independent of  $a$ . While this does not probe the continuum limit of RoM in a physical region, it probes finer components of the wavefunction that cannot be seen with smaller system sizes. Figure 14 shows the RoM of adjacent physical sites (4 qubits)  $\Delta R$  as a function of the position  $n$  and separation of external charges  $d$ . The plots with smaller  $a$  provide a finer, “zoomed in” resolution view into the structure of the states. At  $N = 440, a = 1/2$ , additional structure is seen in  $\Delta R$  between the mesons after the string has broken. Interestingly, this structure resembles the structure in the pressure shown in Fig. 13. The bottom row of Fig. 14 shows the RoM between disjoint regions of the lattice as a function of separation (defined in Eq. (20))  $\Delta R_{AB}$ , scaled by  $a$ . The structure initially present in the  $N = 220, a = 1$  data is seen to vanish as  $a$  is decreased. The fixed-size RoM calculation (4 qubits) shows less information for finer  $a$  because the wavefunction is spread over more lattice sites. Instead, only quasi-local structure (small  $r$ ) remains.

Figure 15 details the behavior of the quantum complexity as  $m/g$  is varied. We consider several values of  $m$  holding  $g$  fixed as in the main text, and expand the lattice to account for the increased correlation length with smaller mass. The top and middle rows, as in Fig. 6, display the RoM between adjacent sites,  $\Delta R$ , and the charge density  $q_n$  as a function of position  $n$  and separation  $d$ . The transition from strings to mesons becomes increasingly sharper with larger  $m/g$ , which is seen in both  $\Delta R$  and  $q_n$ . The string also appears to break at a larger separation  $d$  for larger  $m/g$ . This is an expected result of fermions being more “expensive” to excite from the vacuum to screen the external charges. The bottom row, as in Fig. 14, shows the RoM between disjoint  $\Delta R_{AB}$  subsystems on the lattice as a function of the distance between the regions  $r$ . Region  $A$  is at the center of the lattice, and region  $B$  is distance  $r$  away. The vacuum-subtracted  $\Delta R_{AB}$  only shows structure at small  $r$  for the massless case, consistent with the system only having short-range quantum correlations before string breaking. At intermediate  $m/g$ , the correlations before string breaking are longest-range, and then die off again at  $m/g = 1$ . The propagation of the bound hadrons is seen in all parameters besides the massless case.

#### Appendix F: Computational Methods

The reduced density matrix  $\hat{\rho}_{AB}$  is required for the nonlocal measures of complexity such as MI and RoM, where regions  $A, B$  may be separated on the lattice. To avoid exponentially-scaling resource requirements for creating a long-distance reduced density matrix, we apply a swap network to the MPS to move region  $B$  next to region  $A$ , and

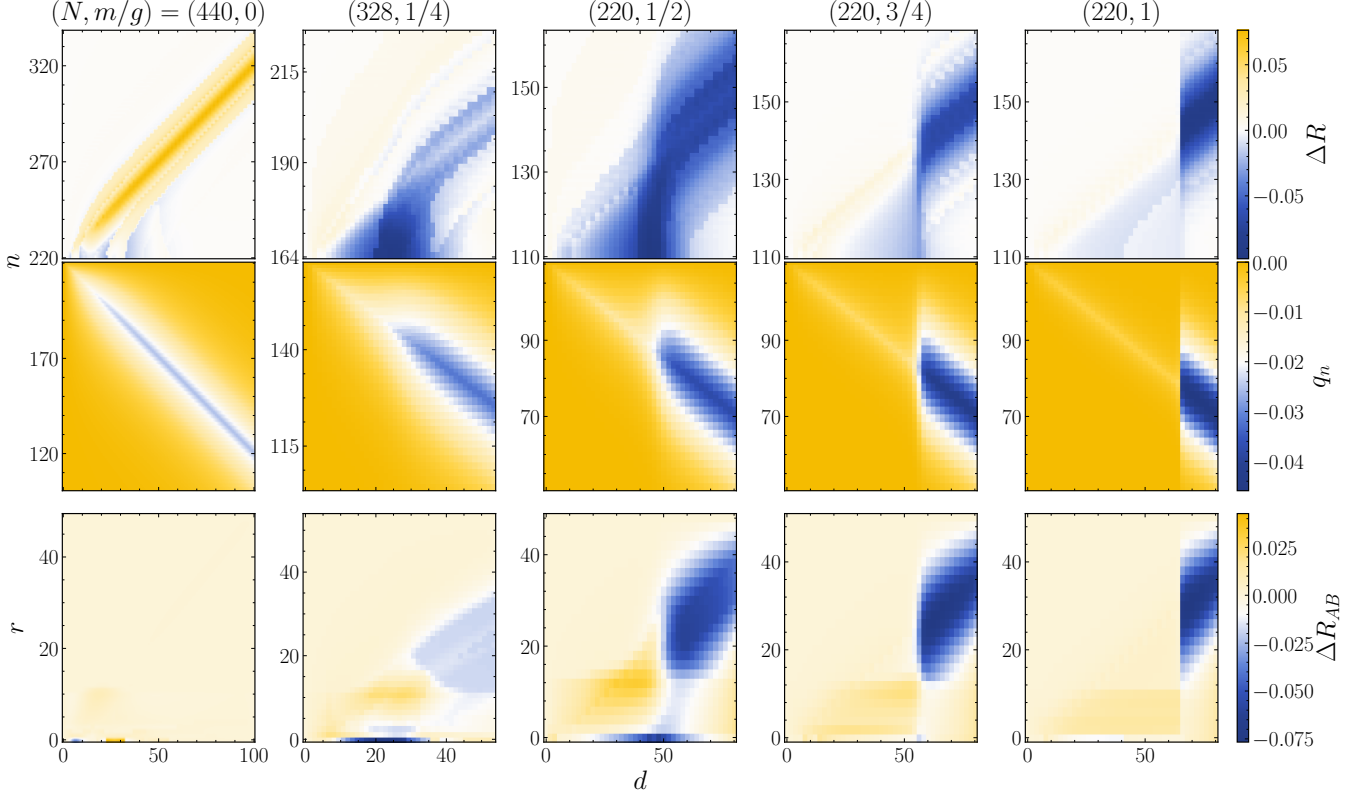


FIG. 15. The dependence of the RoM breaking on fermion mass for a selection of masses,  $m/g = 0$  (first column),  $m/g = 1/4$  (second column),  $m/g = 1/2$  (third column),  $m/g = 3/4$  (fourth column) and  $m/g = 1$  (fifth column). Top: the local vacuum-subtracted RoM  $R$  as a function of  $d$  for half of the lattice  $n \geq N/2$  with  $a = 1$ . Middle: the associated charge densities for half of the lattice  $n \leq N/2$  for the same parameters. Bottom: the RoM of disjoint regions,  $\Delta R_{AB}$ , with region  $A$  at the center of the lattice and region  $B$  a distance  $r$  away. The vacuum value ( $d = 0$ ) and the value as  $r \rightarrow \infty$  are subtracted. The RoM is plotted in units of  $a$  for the same system parameters.

then trace the regions outside  $A, B$ . This introduces long-range entanglement in the system and has the same cost as exactly contracting the region between  $A$  and  $B$ . We approximate this operation by introducing a bond dimension and cutoff for the swap network operation.

We find ground states and low-lying excited states in MPS with DMRG. We use a bond dimension of 400, a cutoff of  $10^{-12}$  and 40 sweeps. The convergence of our MPS computations, both for DMRG and for computing nonlocal reduced states is verified by examining the results as the precision is increased.

The RoM is calculated using the approach of Ref. [58]. The minimization problem of Eq. (8) is reframed as a sparse linear programming problem,

$$R(\hat{\rho}) = \min_{\mathbf{x}} \left\{ \|\mathbf{x}\|_1 \quad \middle| \quad \hat{A}\mathbf{x} = \mathbf{b} \right\}. \quad (\text{F1})$$

Here the matrix  $\hat{A}$  is defined as  $\hat{A}_{ij} = \text{Tr}(\hat{P}_i \hat{\rho}_{s_j})$ , and  $\mathbf{b}$  is the expansion of the state  $\hat{\rho}$  in the Pauli basis:  $b_i = \text{Tr}(\hat{P}_i \hat{\rho})$ . In practice, this may be readily solved in the following form:

$$\underset{\mathbf{u}}{\text{minimize}} \quad \sum_i u_i, \quad \text{s.t.} \quad \begin{pmatrix} \hat{A} & -\hat{A} \end{pmatrix} \mathbf{u} = \mathbf{b}, \quad u_i \geq 0, \quad (\text{F2})$$

A further simplification developed in Ref. [58] is that only a small fraction of stabilizer states have  $x_i > 0$ , and these are correlated with having large values of the overlap  $|2^{n_Q} \text{Tr}(\hat{\rho}_{s_i} \hat{\rho})|$ . This enables further sparsification of the problem, only retaining a fraction  $K$  of the states  $\hat{\rho}_{s_i}$ . In this work,  $K = 0.05$  of states with the largest overlaps are kept for the optimization problem.

The NL RoM is calculated as the minimum of 100 optimizations as in Eq. (10), each with randomly chosen initial

conditions.

---

[1] D. J. Gross and F. Wilczek, Ultraviolet Behavior of Nonabelian Gauge Theories, *Phys. Rev. Lett.* **30**, 1343 (1973).

[2] H. Politzer, Reliable Perturbative Results for Strong Interactions?, *Phys. Rev. Lett.* **30**, 1346 (1973).

[3] C. N. Yang and R. L. Mills, Conservation of isotopic spin and isotopic gauge invariance, *Phys. Rev.* **96**, 191 (1954).

[4] R. D. Field and R. P. Feynman, A Parametrization of the Properties of Quark Jets, *Nucl. Phys. B* **136**, 1 (1978).

[5] B. Andersson, G. Gustafson, G. Ingelman, and T. Sjöstrand, Parton Fragmentation and String Dynamics, *Phys. Rept.* **97**, 31 (1983).

[6] B. Andersson, *The Lund Model*, Cambridge Monographs on Particle Physics, Nuclear Physics and Cosmology (Cambridge University Press, 1998).

[7] T. Sjöstrand, The PYTHIA Event Generator: Past, Present and Future, *Comput. Phys. Commun.* **246**, 106910 (2020), [arXiv:1907.09874 \[hep-ph\]](https://arxiv.org/abs/1907.09874).

[8] S. Agostinelli *et al.* (GEANT4), GEANT4 - A Simulation Toolkit, *Nucl. Instrum. Meth. A* **506**, 250 (2003).

[9] R. Abir *et al.*, The case for an EIC Theory Alliance: Theoretical Challenges of the EIC, (2023), [arXiv:2305.14572 \[hep-ph\]](https://arxiv.org/abs/2305.14572).

[10] R. Abdul Khalek *et al.*, Science Requirements and Detector Concepts for the Electron-Ion Collider: EIC Yellow Report, *Nucl. Phys. A* **1026**, 122447 (2022), [arXiv:2103.05419 \[physics.ins-det\]](https://arxiv.org/abs/2103.05419).

[11] J. C. Halimeh, N. Mueller, J. Knolle, Z. Papić, and Z. Davoudi, Quantum simulation of out-of-equilibrium dynamics in gauge theories, [arXiv:2509.03586 \[quant-ph\]](https://arxiv.org/abs/2509.03586) (2025).

[12] D. E. Kharzeev, The Maximal Entanglement Limit in Statistical and High Energy Physics (2026) [arXiv:2601.00405 \[quant-ph\]](https://arxiv.org/abs/2601.00405).

[13] C. DeTar, O. Kaczmarek, F. Karsch, and E. Laermann, String breaking in lattice quantum chromodynamics, *Phys. Rev. D* **59**, 031501 (1998).

[14] S. Aoki *et al.* (CP-PACS), The Static quark potential in full QCD, *Nucl. Phys. B Proc. Suppl.* **73**, 216 (1999), [arXiv:hep-lat/9809185](https://arxiv.org/abs/hep-lat/9809185).

[15] SESAM, G. Bali, N. Eicker, L. Giusti, U. Glässner, S. Guesken, H. Hoeber, P. Lacock, T. Lippert, G. Martinelli, F. Rapuano, G. Ritzenhöfer, K. Schilling, G. Siegert, A. Spitz, P. Ueberholz, and J. Viehoff, Glueballs and string breaking from full qcd, *Nuclear Physics B - Proceedings Supplements* **63**, 209 (1998), proceedings of the XVth International Symposium on Lattice Field Theory.

[16] G. S. Bali, H. Neff, T. Duessel, T. Lippert, and K. Schilling (SESAM), Observation of string breaking in QCD, *Phys. Rev. D* **71**, 114513 (2005), [arXiv:hep-lat/0505012](https://arxiv.org/abs/hep-lat/0505012).

[17] P. Pennanen and C. Michael (UKQCD), String breaking in zero temperature lattice QCD, [arXiv:hep-lat/0001015](https://arxiv.org/abs/hep-lat/0001015) (2000).

[18] A. Duncan, E. Eichten, and H. Thacker, String breaking in four dimensional lattice qcd, *Phys. Rev. D* **63**, 111501 (2001).

[19] J. Bulava, B. Hörz, F. Knechtli, V. Koch, G. Moir, C. Morningstar, and M. Peardon, String breaking by light and strange quarks in QCD, *Phys. Lett. B* **793**, 493 (2019), [arXiv:1902.04006 \[hep-lat\]](https://arxiv.org/abs/1902.04006).

[20] B. Buyens, J. Haegeman, H. Verschelde, F. Verstraete, and K. Van Acoleyen, Confinement and string breaking for QED<sub>2</sub> in the Hamiltonian picture, *Phys. Rev. X* **6**, 041040 (2016), [arXiv:1509.00246 \[hep-lat\]](https://arxiv.org/abs/1509.00246).

[21] S. Grieninger, D. E. Kharzeev, and E. Marroquin, Thermal nature of confining strings, (2025), [arXiv:2510.23919 \[hep-ph\]](https://arxiv.org/abs/2510.23919).

[22] A. Florio, D. Frenklakh, S. Grieninger, D. E. Kharzeev, A. Palermo, and S. Shi, Thermalization from quantum entanglement: Jet simulations in the massive schwinger model, *Phys. Rev. D* **112**, 094502 (2025).

[23] A. Florio, D. Frenklakh, K. Ikeda, D. Kharzeev, V. Korepin, S. Shi, and K. Yu, Real-Time Nonperturbative Dynamics of Jet Production in Schwinger Model: Quantum Entanglement and Vacuum Modification, *Phys. Rev. Lett.* **131**, 021902 (2023), [arXiv:2301.11991 \[hep-ph\]](https://arxiv.org/abs/2301.11991).

[24] A. Florio, D. Frenklakh, K. Ikeda, D. E. Kharzeev, V. Korepin, S. Shi, and K. Yu, Quantum real-time evolution of entanglement and hadronization in jet production: Lessons from the massive Schwinger model, *Phys. Rev. D* **110**, 094029 (2024), [arXiv:2404.00087 \[hep-ph\]](https://arxiv.org/abs/2404.00087).

[25] R. A. Janik, M. A. Nowak, M. M. Rams, and I. Zahed, Emergent Nonthermal Fluid from Jets in the Massive Schwinger Model Using Tensor Networks, *Phys. Rev. Lett.* **135**, 211903 (2025), [arXiv:2502.12901 \[hep-ph\]](https://arxiv.org/abs/2502.12901).

[26] J. Barata and E. Rico, Real-time simulation of jet energy loss and entropy production in high-energy scattering with matter, [arXiv:2502.17558 \[hep-ph\]](https://arxiv.org/abs/2502.17558) (2025).

[27] C. Artiaco, J. Barata, and E. Rico, Out-of-Equilibrium Dynamics in a U(1) Lattice Gauge Theory via Local Information Flows: Scattering and String Breaking, [arXiv:2510.16101 \[quant-ph\]](https://arxiv.org/abs/2510.16101) (2025).

[28] R. Verdel, F. Liu, S. Whitsitt, A. V. Gorshkov, and M. Heyl, Real-time dynamics of string breaking in quantum spin chains, *Phys. Rev. B* **102**, 014308 (2020), [arXiv:1911.11382 \[cond-mat.stat-mech\]](https://arxiv.org/abs/1911.11382).

[29] R. Verdel, G.-Y. Zhu, and M. Heyl, Dynamical Localization Transition of String Breaking in Quantum Spin Chains, *Phys. Rev. Lett.* **131**, 230402 (2023), [arXiv:2304.12957 \[cond-mat.str-el\]](https://arxiv.org/abs/2304.12957).

[30] A. Mallick, M. Lewenstein, J. Zakrzewski, and M. Płodzień, String-breaking dynamics in an Ising chain with local vibrations, *Phys. Rev. B* **112**, 024311 (2025), [arXiv:2501.00604 \[quant-ph\]](https://arxiv.org/abs/2501.00604).

[31] T. A. Cochran *et al.*, Visualizing dynamics of charges and strings in (2 + 1)D lattice gauge theories, *Nature* **642**, 315 (2025), [arXiv:2409.17142 \[quant-ph\]](https://arxiv.org/abs/2409.17142).

[32] D. Gonzalez-Cuadra *et al.*, Observation of string breaking on a (2 + 1)D Rydberg quantum simulator, *Nature* **642**, 321 (2025), arXiv:2410.16558 [quant-ph].

[33] U. Borla, J. J. Osborne, S. Moroz, and J. C. Halimeh, String Breaking in a 2 + 1D  $\mathbb{Z}_2$  Lattice Gauge Theory, arXiv:2501.17929 [quant-ph] (2025).

[34] G. Cataldi, S. Orlando, and J. C. Halimeh, Real-Time String Dynamics in a 2 + 1D Non-Abelian Lattice Gauge Theory: String Breaking, Glueball Formation, Baryon Blockade, and Tension Reduction, arXiv:2509.08868 [hep-lat] (2025).

[35] K. Xu, U. Borla, S. Moroz, and J. C. Halimeh, String Breaking Dynamics and Glueball Formation in a 2 + 1D Lattice Gauge Theory, arXiv:2507.01950 [hep-lat] (2025).

[36] F. Di Marcantonio, S. Pradhan, S. Vallecorsa, M. C. Bañuls, and E. R. Ortega, Roughening and dynamics of an electric flux string in a (2+1)D lattice gauge theory, arXiv:2505.23853 [hep-lat] (2025).

[37] A. N. Ciavarella and C. W. Bauer, Quantum Simulation of SU(3) Lattice Yang-Mills Theory at Leading Order in Large-Nc Expansion, *Phys. Rev. Lett.* **133**, 111901 (2024), arXiv:2402.10265 [hep-ph].

[38] A. N. Ciavarella and C. W. Bauer, Quantum Simulation of Large N Lattice Gauge Theories, *PoS LATTICE2024*, 206 (2025), arXiv:2411.16704 [hep-lat].

[39] A. Crippa, K. Jansen, and E. Rinaldi, Analysis of the confinement string in (2 + 1)-dimensional Quantum Electrodynamics with a trapped-ion quantum computer, arXiv:2411.05628 [hep-lat] (2024).

[40] Y. Liu, W.-Y. Zhang, Z.-H. Zhu, M.-G. He, Z.-S. Yuan, and J.-W. Pan, String-Breaking Mechanism in a Lattice Schwinger Model Simulator, *Phys. Rev. Lett.* **135**, 101902 (2025), arXiv:2411.15443 [cond-mat.quant-gas].

[41] A. De *et al.*, Observation of string-breaking dynamics in a quantum simulator, arXiv:2410.13815 [quant-ph] (2024).

[42] F. M. Surace *et al.*, String-Breaking Dynamics in Quantum Adiabatic and Diabatic Processes, arXiv:2411.10652 [quant-ph] (2024).

[43] A. N. Ciavarella, String breaking in the heavy quark limit with scalable circuits, *Phys. Rev. D* **111**, 054501 (2025), arXiv:2411.05915 [quant-ph].

[44] C. Alexandrou, A. Athenodorou, K. Blekos, G. Polykratis, and S. Kühn, Realizing string breaking dynamics in a  $Z_2$  lattice gauge theory on quantum hardware, arXiv:2504.13760 [hep-lat] (2025).

[45] D. Luo *et al.*, Quantum simulation of bubble nucleation across a quantum phase transition, arXiv:2505.09607 [quant-ph] (2025).

[46] J. Haferkamp, P. Faist, N. B. T. Kothakonda, J. Eisert, and N. Y. Halpern, Linear growth of quantum circuit complexity, *Nature Phys.* **18**, 528 (2022), arXiv:2106.05305 [quant-ph].

[47] E. Chitambar and G. Gour, Quantum resource theories, *Rev. Mod. Phys.* **91**, 025001 (2019), arXiv:1806.06107 [quant-ph].

[48] A. R. Brown and L. Susskind, Second law of quantum complexity, *Phys. Rev. D* **97**, 086015 (2018), arXiv:1701.01107 [hep-th].

[49] J. Eisert, M. Cramer, and M. B. Plenio, Area laws for the entanglement entropy - a review, *Rev. Mod. Phys.* **82**, 277 (2010), arXiv:0808.3773 [quant-ph].

[50] L. Leone, S. F. E. Oliviero, and A. Hamma, Stabilizer Rényi Entropy, *Phys. Rev. Lett.* **128**, 050402 (2022), arXiv:2106.12587 [quant-ph].

[51] C. Robin, M. J. Savage, and N. Pillet, Entanglement Rearrangement in Self-Consistent Nuclear Structure Calculations, *Phys. Rev. C* **103**, 034325 (2021), arXiv:2007.09157 [nucl-th].

[52] T. Haug and L. Piroli, Stabilizer entropies and nonstabilizerness monotones, *Quantum* **7**, 1092 (2023), arXiv:2303.10152 [quant-ph].

[53] P. S. Tarabunga, Critical behaviors of non-stabilizerness in quantum spin chains, *Quantum* **8**, 1413 (2024), arXiv:2309.00676 [quant-ph].

[54] S. M. Hengstenberg, C. E. P. Robin, and M. J. Savage, Multi-body entanglement and information rearrangement in nuclear many-body systems: a study of the Lipkin–Meshkov–Glick model, *Eur. Phys. J. A* **59**, 231 (2023), arXiv:2306.16535 [nucl-th].

[55] T. Haug, L. Aolita, and M. S. Kim, Probing quantum complexity via universal saturation of stabilizer entropies, *Quantum* **9**, 1801 (2025), arXiv:2406.04190 [quant-ph].

[56] J. Emerson, D. Gottesman, S. A. H. Mousavian, and V. Veitch, The resource theory of stabilizer quantum computation, *New J. Phys.* **16**, 013009 (2014), arXiv:1307.7171 [quant-ph].

[57] M. Howard and E. T. Campbell, Application of a Resource Theory for Magic States to Fault-Tolerant Quantum Computing, *Phys. Rev. Lett.* **118**, 090501 (2017), arXiv:1609.07488 [quant-ph].

[58] H. Hamaguchi, K. Hamada, and N. Yoshioka, Handbook for Efficiently Quantifying Robustness of Magic, *Quantum* **8**, 1461 (2024), arXiv:2311.01362 [quant-ph].

[59] E. Tirrito, P. S. Tarabunga, G. Lami, T. Chanda, L. Leone, S. F. E. Oliviero, M. Dalmonte, M. Collura, and A. Hamma, Quantifying nonstabilizerness through entanglement spectrum flatness, *Phys. Rev. A* **109**, L040401 (2024), arXiv:2304.01175 [quant-ph].

[60] I. Chernyshev, C. E. P. Robin, and M. J. Savage, Quantum magic and computational complexity in the neutrino sector, *Phys. Rev. Res.* **7**, 023228 (2025), arXiv:2411.04203 [quant-ph].

[61] C. Cao, G. Cheng, A. Hamma, L. Leone, W. Munizzi, and S. F. E. Oliviero, Gravitational Backreaction is Magical, *PRX Quantum* **6**, 040375 (2025), arXiv:2403.07056 [hep-th].

[62] C. E. P. Robin and M. J. Savage, Quantum complexity fluctuations from nuclear and hypernuclear forces, *Phys. Rev. C* **112**, 044004 (2025), arXiv:2405.10268 [nucl-th].

[63] F. Brökmeyer, S. M. Hengstenberg, J. W. Keeble, C. E. Robin, F. Rocco, and M. J. Savage, Quantum magic and multipartite entanglement in the structure of nuclei, *Physical Review C* **111**, 034317 (2025).

[64] C. E. P. Robin and M. J. Savage, Anti-Flatness and Non-Local Magic in Two-Particle Scattering Processes, (2025), [arXiv:2510.23426 \[quant-ph\]](https://arxiv.org/abs/2510.23426).

[65] X. Jiang, J. C. Halimeh, and N. S. Srivatsa, Krylov Complexity Meets Confinement, (2025), [arXiv:2511.03783 \[cond-mat.stat-mech\]](https://arxiv.org/abs/2511.03783).

[66] S. Kühn, J. I. Cirac, and M.-C. Bañuls, Quantum simulation of the schwinger model: A study of feasibility, *Phys. Rev. A* **90**, 042305 (2014).

[67] C. Muschik, M. Heyl, E. Martinez, T. Monz, P. Schindler, B. Vogell, M. Dalmonte, P. Hauke, R. Blatt, and P. Zoller, U(1) Wilson lattice gauge theories in digital quantum simulators, *New J. Phys.* **19**, 103020 (2017), [arXiv:1612.08653 \[quant-ph\]](https://arxiv.org/abs/1612.08653).

[68] N. Klco, E. F. Dumitrescu, A. J. McCaskey, T. D. Morris, R. C. Pooser, M. Sanz, E. Solano, P. Lougovski, and M. J. Savage, Quantum-classical computation of Schwinger model dynamics using quantum computers, *Phys. Rev. A* **98**, 032331 (2018), [arXiv:1803.03326 \[quant-ph\]](https://arxiv.org/abs/1803.03326).

[69] R. C. Farrell, M. Illa, A. N. Ciavarella, and M. J. Savage, Scalable Circuits for Preparing Ground States on Digital Quantum Computers: The Schwinger Model Vacuum on 100 Qubits, *PRX Quantum* **5**, 020315 (2024), [arXiv:2308.04481 \[quant-ph\]](https://arxiv.org/abs/2308.04481).

[70] R. C. Farrell, M. Illa, A. N. Ciavarella, and M. J. Savage, Quantum simulations of hadron dynamics in the Schwinger model using 112 qubits, *Phys. Rev. D* **109**, 114510 (2024), [arXiv:2401.08044 \[quant-ph\]](https://arxiv.org/abs/2401.08044).

[71] N. H. Nguyen, M. C. Tran, Y. Zhu, A. M. Green, C. H. Alderete, Z. Davoudi, and N. M. Linke, Digital Quantum Simulation of the Schwinger Model and Symmetry Protection with Trapped Ions, *PRX Quantum* **3**, 020324 (2022), [arXiv:2112.14262 \[quant-ph\]](https://arxiv.org/abs/2112.14262).

[72] J. B. Kogut and L. Susskind, Hamiltonian Formulation of Wilson's Lattice Gauge Theories, *Phys. Rev. D* **11**, 395 (1975).

[73] T. Banks, L. Susskind, and J. B. Kogut, Strong Coupling Calculations of Lattice Gauge Theories: (1+1)-Dimensional Exercises, *Phys. Rev. D* **13**, 1043 (1976).

[74] L. Susskind, Lattice Fermions, *Phys. Rev. D* **16**, 3031 (1977).

[75] P. Jordan and E. P. Wigner, About the Pauli exclusion principle, *Z. Phys.* **47**, 631 (1928).

[76] E. H. Lieb, T. Schultz, and D. Mattis, Two soluble models of an antiferromagnetic chain, *Annals Phys.* **16**, 407 (1961).

[77] R. Dempsey, I. R. Klebanov, S. S. Pufu, and B. Zan, Discrete chiral symmetry and mass shift in the lattice Hamiltonian approach to the Schwinger model, *Phys. Rev. Res.* **4**, 043133 (2022), [arXiv:2206.05308 \[hep-th\]](https://arxiv.org/abs/2206.05308).

[78] K. Huang and C. N. Yang, Quantum-mechanical many-body problem with hard-sphere interaction, *Phys. Rev.* **105**, 767 (1957).

[79] H. W. Hamber, E. Marinari, G. Parisi, and C. Rebbi, Considerations on Numerical Analysis of QCD, *Nucl. Phys. B* **225**, 475 (1983).

[80] M. Luscher, Volume Dependence of the Energy Spectrum in Massive Quantum Field Theories. 2. Scattering States, *Commun. Math. Phys.* **105**, 153 (1986).

[81] M. Luscher, Two particle states on a torus and their relation to the scattering matrix, *Nucl. Phys. B* **354**, 531 (1991).

[82] M. Luscher and U. Wolff, How to Calculate the Elastic Scattering Matrix in Two-dimensional Quantum Field Theories by Numerical Simulation, *Nucl. Phys. B* **339**, 222 (1990).

[83] W. Detmold, K. Orginos, and M. J. Savage, BB Potentials in Quenched Lattice QCD, *Phys. Rev. D* **76**, 114503 (2007), [arXiv:hep-lat/0703009](https://arxiv.org/abs/hep-lat/0703009).

[84] H.-H. Lu *et al.*, Simulations of Subatomic Many-Body Physics on a Quantum Frequency Processor, *Phys. Rev. A* **100**, 012320 (2019), [arXiv:1810.03959 \[quant-ph\]](https://arxiv.org/abs/1810.03959).

[85] R. A. Briceno, Z. Davoudi, T. C. Luu, and M. J. Savage, Two-Baryon Systems with Twisted Boundary Conditions, *Phys. Rev. D* **89**, 074509 (2014), [arXiv:1311.7686 \[hep-lat\]](https://arxiv.org/abs/1311.7686).

[86] S. Ghosh, R. M. Soni, and S. P. Trivedi, On The Entanglement Entropy For Gauge Theories, *JHEP* **09**, 069, [arXiv:1501.02593 \[hep-th\]](https://arxiv.org/abs/1501.02593).

[87] X. Turkeshi, P. Ruggiero, V. Alba, and P. Calabrese, Entanglement equipartition in critical random spin chains, *Phys. Rev. B* **102**, 014455 (2020), [arXiv:2005.03331 \[cond-mat.stat-mech\]](https://arxiv.org/abs/2005.03331).

[88] P. V. Buividovich and M. I. Polikarpov, Entanglement entropy in gauge theories and the holographic principle for electric strings, *Phys. Lett. B* **670**, 141 (2008), [arXiv:0806.3376 \[hep-th\]](https://arxiv.org/abs/0806.3376).

[89] W. Donnelly, Decomposition of entanglement entropy in lattice gauge theory, *Phys. Rev. D* **85**, 085004 (2012), [arXiv:1109.0036 \[hep-th\]](https://arxiv.org/abs/1109.0036).

[90] H. Casini, M. Huerta, and J. A. Rosabal, Remarks on entanglement entropy for gauge fields, *Phys. Rev. D* **89**, 085012 (2014), [arXiv:1312.1183 \[hep-th\]](https://arxiv.org/abs/1312.1183).

[91] D. Radicevic, Notes on Entanglement in Abelian Gauge Theories, (2014), [arXiv:1404.1391 \[hep-th\]](https://arxiv.org/abs/1404.1391).

[92] S. Aoki, T. Iritani, M. Nozaki, T. Numasawa, N. Shiba, and H. Tasaki, On the definition of entanglement entropy in lattice gauge theories, *JHEP* **06**, 187, [arXiv:1502.04267 \[hep-th\]](https://arxiv.org/abs/1502.04267).

[93] R. M. Soni and S. P. Trivedi, Entanglement entropy in (3 + 1)-d free U(1) gauge theory, *JHEP* **02**, 101, [arXiv:1608.00353 \[hep-th\]](https://arxiv.org/abs/1608.00353).

[94] M. Goldstein and E. Sela, Symmetry-resolved entanglement in many-body systems, *Phys. Rev. Lett.* **120**, 200602 (2018), [arXiv:1711.09418 \[cond-mat.stat-mech\]](https://arxiv.org/abs/1711.09418).

[95] T. Nishioka, Entanglement entropy: holography and renormalization group, *Rev. Mod. Phys.* **90**, 035007 (2018), [arXiv:1801.10352 \[hep-th\]](https://arxiv.org/abs/1801.10352).

[96] R. Amorosso, S. Syritsyn, and R. Venugopalan, Entanglement entropy of a color flux tube in (2+1)D Yang-Mills theory, *JHEP* **12**, 177, [arXiv:2410.00112 \[hep-lat\]](https://arxiv.org/abs/2410.00112).

[97] R. Amorosso, S. Syritsyn, and R. Venugopalan, Entanglement entropy of a color flux tube in (1+1)D Yang–Mills theory, *Phys. Lett. B* **868**, 139806 (2025), [arXiv:2411.12818 \[hep-lat\]](https://arxiv.org/abs/2411.12818).

[98] H. Zhu, R. Kueng, M. Grassl, and D. Gross, The clifford group fails gracefully to be a unitary 4-design (2016), [arXiv:1609.08172 \[quant-ph\]](https://arxiv.org/abs/1609.08172).

[99] P. R. N. Falcão, P. S. Tarabunga, M. Frau, E. Tirrito, J. Zakrzewski, and M. Dalmonte, Nonstabilizerness in U(1) lattice gauge theory, *Phys. Rev. B* **111**, L081102 (2025), [arXiv:2409.01789 \[quant-ph\]](https://arxiv.org/abs/2409.01789).

[100] F.-K. Guo, C. Hanhart, U.-G. Meißner, Q. Wang, Q. Zhao, and B.-S. Zou, Hadronic molecules, *Rev. Mod. Phys.* **90**, 015004 (2018), [Erratum: *Rev.Mod.Phys.* 94, 029901 (2022)], [arXiv:1705.00141 \[hep-ph\]](https://arxiv.org/abs/1705.00141).

[101] L. Ebner, B. Müller, A. Schäfer, L. Schmotzer, C. Seidl, and X. Yao, The Magic Barrier before Thermalization, (2025), [arXiv:2510.11681 \[quant-ph\]](https://arxiv.org/abs/2510.11681).

[102] A. Wong and N. Christensen, Potential multiparticle entanglement measure, *Phys. Rev. A* **63**, 044301 (2001).

[103] D. Qian and J. Wang, Quantum nonlocal nonstabilizerness, *Phys. Rev. A* **111**, 052443 (2025), [arXiv:2502.06393 \[quant-ph\]](https://arxiv.org/abs/2502.06393).

[104] N. A. Zemlevskiy, Scalable quantum simulations of scattering in scalar field theory on 120 qubits, *Phys. Rev. D* **112**, 034502 (2025), [arXiv:2411.02486 \[quant-ph\]](https://arxiv.org/abs/2411.02486).

[105] R. C. Farrell, N. A. Zemlevskiy, M. Illa, and J. Preskill, Digital quantum simulations of scattering in quantum field theories using W states, (2025), [arXiv:2505.03111 \[quant-ph\]](https://arxiv.org/abs/2505.03111).

[106] R. C. Farrell, M. Illa, and M. J. Savage, Steps toward quantum simulations of hadronization and energy loss in dense matter, *Phys. Rev. C* **111**, 015202 (2025), [arXiv:2405.06620 \[quant-ph\]](https://arxiv.org/abs/2405.06620).

[107] Z. Li, M. Illa, and M. J. Savage, A Framework for Quantum Simulations of Energy-Loss and Hadronization in Non-Abelian Gauge Theories: SU(2) Lattice Gauge Theory in 1+1D, (2025), [arXiv:2512.05210 \[quant-ph\]](https://arxiv.org/abs/2512.05210).

[108] C. D. White and M. J. White, Magic states of top quarks, *Phys. Rev. D* **110**, 116016 (2024), [arXiv:2406.07321 \[hep-ph\]](https://arxiv.org/abs/2406.07321).

[109] E. Yazgan (CMS Collaboration), Measurements of top quark properties in CMS:  $t\bar{t}$  spin density matrix, quantum entanglement and quantum magic, in *2025 European Physical Society Conference on High Energy Physics* (2025) [arXiv:2510.13743 \[hep-ex\]](https://arxiv.org/abs/2510.13743).

[110] R. Pordes, D. Petravick, B. Kramer, D. Olson, M. Livny, A. Roy, P. Avery, K. Blackburn, T. Wenaus, F. Würthwein, I. Foster, R. Gardner, M. Wilde, A. Blatecky, J. McGee, and R. Quick, The open science grid, in *J. Phys. Conf. Ser.*, 78, Vol. 78 (2007) p. 012057.

[111] I. Sfiligoi, D. C. Bradley, B. Holzman, P. Mhashilkar, S. Padhi, and F. Wurthwein, The pilot way to grid resources using glideinwms, in *2009 WRI World Congress on Computer Science and Information Engineering*, 2, Vol. 2 (2009) pp. 428–432.

[112] OSG, [Ospool](https://osgpool.org) (2006).

[113] OSG, [Open science data federation](https://osg.org) (2015).

[114] M. Fishman, S. R. White, and E. M. Stoudenmire, The ITensor Software Library for Tensor Network Calculations, *SciPost Phys. Codebases* , 4 (2022).

[115] M. Fishman, S. R. White, and E. M. Stoudenmire, Codebase release 0.3 for ITensor, *SciPost Phys. Codebases* , 4 (2022).

[116] B. Corbett and A. Miyake, Scaling up the transcorrelated density matrix renormalization group, *Phys. Rev. B* **112**, 165120 (2025), [arXiv:2506.07441 \[cond-mat.str-el\]](https://arxiv.org/abs/2506.07441).

[117] F. Verstraete, D. Porras, and J. I. Cirac, Density matrix renormalization group and periodic boundary conditions: A quantum information perspective, *Phys. Rev. Lett.* **93**, 227205 (2004).

[118] T. V. Zache, N. Mueller, J. T. Schneider, F. Jendrzejewski, J. Berges, and P. Hauke, Dynamical topological transitions in the massive Schwinger model with a  $\theta$ -term, *Phys. Rev. Lett.* **122**, 050403 (2019), [arXiv:1808.07885 \[quant-ph\]](https://arxiv.org/abs/1808.07885).

[119] T. V. Zache, *Quantum simulation of high-energy physics with ultracold atoms.*, Ph.D. thesis, U. Heidelberg (main) (2020).

[120] S. Grieninger, J. Montgomery, F. Ringer, and I. Zahed, Tensor network simulations of quasi-GPDs in the massive Schwinger model, (2025), [arXiv:2511.17752 \[hep-lat\]](https://arxiv.org/abs/2511.17752).

[121] S. Aaronson and D. Gottesman, Improved simulation of stabilizer circuits, *Phys. Rev. A* **70**, 052328 (2004), [arXiv:quant-ph/0406196](https://arxiv.org/abs/quant-ph/0406196).